(12) INTERNATIONAL APPLICATION PUBLISHED UNDER THE PATENT COOPERATION TREATY (PCT)

(19) World Intellectual Property Organization
International Bureau

(43) International Publication Date
29 October 2015 (29.10.2015)

WIPO | PCT

(10) International Publication Number
WO 2015/163958 A2

(51) International Patent Classification:
G02B 6/12 (2006.01)

(21) International Application Number:
PCT/US2015/014105

(22) International Filing Date:
2 February 2015 (02.02.2015)

(25) Filing Language: English

(26) Publication Language: English

(30) Priority Data:
61/934,511 31 January 2014 (31.01.2014) US

(71) Applicant: **PRESIDENT AND FELLOWS OF HARVARD COLLEGE** [US/US]; 17 Quincy Street, Cambridge, Massachusetts 02138 (US).

(72) Inventors: **MAZUR, Eric**; 57 Lowell Road, Concord, Massachusetts 01742 (US). **LI, Yang**; 81 Marion St., 3rd Floor, Somerville, Massachusetts 02143 (US). **RESHEF, Orad**; 2443 Massachusetts Avenue, Cambridge, Massachusetts 02140 (US). **LONCAR, Marko**; 153 Claflin Street, Belmont, Massachusetts 02478 (US). **KITA, Shota**; 81 Marion St., 3rd Floor, Cambridge, Massachusetts 02143 (US). **MUNOZ, Philip Alejandro**; 78 Spring Street, Cambridge, Massachusetts 02138 (US). **VULIS, Daryl, Inna**; 24 Peabody Terrace, Cambridge, Massachusetts 02138 (US).

(74) Agent: **MOLLAAGHABABA, Reza**; Pepper Hamilton LLP, 19th Floor, High Street Tower, 125 High Street, Boston, Massachusetts 02110-2736 (US).

(81) Designated States *(unless otherwise indicated, for every kind of national protection available)*: AE, AG, AL, AM, AO, AT, AU, AZ, BA, BB, BG, BH, BN, BR, BW, BY, BZ, CA, CH, CL, CN, CO, CR, CU, CZ, DE, DK, DM, DO, DZ, EC, EE, EG, ES, FI, GB, GD, GE, GH, GM, GT, HN, HR, HU, ID, IL, IN, IR, IS, JP, KE, KG, KN, KP, KR, KZ, LA, LC, LK, LR, LS, LU, LY, MA, MD, ME, MG, MK, MN, MW, MX, MY, MZ, NA, NG, NI, NO, NZ, OM, PA, PE, PG, PH, PL, PT, QA, RO, RS, RU, RW, SA, SC, SD, SE, SG, SK, SL, SM, ST, SV, SY, TH, TJ, TM, TN, TR, TT, TZ, UA, UG, US, UZ, VC, VN, ZA, ZM, ZW.

(84) Designated States *(unless otherwise indicated, for every kind of regional protection available)*: ARIPO (BW, GH, GM, KE, LR, LS, MW, MZ, NA, RW, SD, SL, ST, SZ, TZ, UG, ZM, ZW), Eurasian (AM, AZ, BY, KG, KZ, RU, TJ, TM), European (AL, AT, BE, BG, CH, CY, CZ, DE, DK, EE, ES, FI, FR, GB, GR, HR, HU, IE, IS, IT, LT, LU, LV, MC, MK, MT, NL, NO, PL, PT, RO, RS, SE, SI, SK, SM, TR), OAPI (BF, BJ, CF, CG, CI, CM, GA, GN, GQ, GW, KM, ML, MR, NE, SN, TD, TG).

[Continued on next page]

(54) Title: INTEGRATED IMPEDANCE-MATCHED PHOTONIC ZERO-INDEX METAMATERIALS

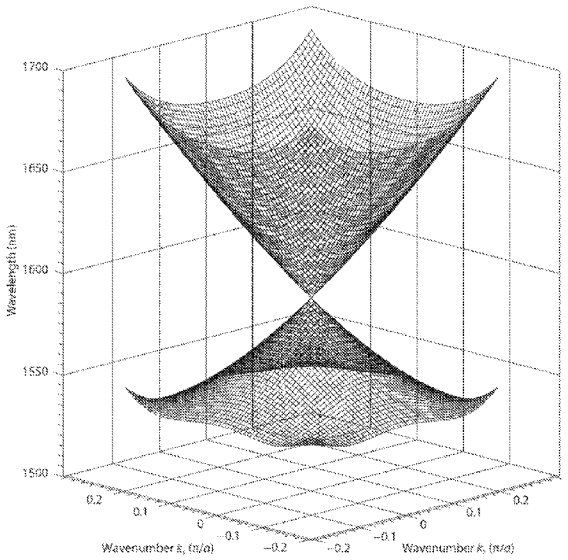

FIG. 23

(57) Abstract: In one aspect, a composition of matter is disclosed, which comprises a photonic crystal comprising a plurality of 2D or 3D periodically repeating structures, where the structures are configured and arranged relative to one another such that the photonic crystal exhibits a Dirac cone at the center of the Brillouin zone of its reciprocal lattice, e.g., at one frequency in the optical regime. In some embodiments, the structures are formed of a dielectric material.

WO 2015/163958 A2

Published:

— *without international search report and to be republished upon receipt of that report (Rule 48.2(g))*

INTEGRATED IMPEDANCE-MATCHED PHOTONIC ZERO-INDEX METAMATERIALS

Cross-Reference to Related Application

This application claims the benefit of priority of U.S. Provisional Application No. 61/934,511 filed January 31, 2014, which is hereby incorporated by reference in its entirety.

Federally Sponsored Research

This invention was made with Government support under grant DMR-1360889 awarded by National Science Foundation (NSF). The Government has certain rights in the invention.

Background

The present invention relates generally to photonic crystals that exhibit a substantially vanishing refractive index and a finite impedance, and more particularly to photonic crystals that exhibit such properties for one or more frequencies in the optical regime.

The field of metamaterials has received a great deal of attention and has progressed rapidly over the last decade The earliest and most cited property of metamaterials, i.e., negative refractive index, has already been demonstrated in potential applications in superlens imaging and rainbow-trapping. Another exotic property, zero refractive index, can be employed in supercoupling and cloaking applications. For example, using an anisotropic positive refractive index from zero to one, a cloak can be built based on transformation optics.

At present, the negative/zero/positive refractive index is usually achieved by following well-established physical principles: 1) plasmonics; 2) metallic resonators; 3) periodically L-C loaded transmission lines; and 4) dielectric resonators.

For example, in some conventional metamaterials, to realize a zero refractive index for a specific wavelength λ, a periodic array of scatters is employed, each of which generates an

electric or magnetic flux loop. The scatters are configured such that the flux loops are canceled by those of neighboring scatters due to multiple interferences, thus achieving $\varepsilon_{eff} = 0$ or $\mu_{eff} = 0$ effectively, resulting in a zero effective index ($n_{eff} = (\varepsilon_{eff} \cdot \mu_{eff})^{1/2} = 0$). However, such structures exhibit infinite or zero impedance $(\mu_{eff}/\varepsilon_{eff})^{1/2}$ for the propagation of electromagnetic waves. As such, electromagnetic waves cannot be coupled into such conventional zero-index metamaterials (ZIM) from free space or waveguide structures without implementing a specific impedance matching technique.

Thus, the conventional metamaterials can have certain shortcomings. For example, the negative (zero) refractive index provided by plasmonics, metallic, and Mie-resonance-based non-metallic metamaterials is usually associated with high losses and mismatched impedance. These drawbacks decrease the performance of those metamaterials dramatically so as to limit their potential applications.

Accordingly, there is a need for enhanced metamaterials exhibiting, e.g., zero or negative, indices of refraction, and concurrently exhibiting a finite impedance.

Summary

In one aspect, a composition of matter is disclosed, which comprises a photonic crystal comprising a plurality of 2D or 3D periodically repeating structures, where the structures are configured and arranged relative to one another such that the photonic crystal exhibits a Dirac cone at the center of the Brillouin zone of its reciprocal lattice, e.g., at one frequency in the optical regime. In some embodiments, the structures are formed of a dielectric material.

In some embodiments, the repeating structures comprise a 2D arrangement of a plurality of pillars. In some embodiments, the pillars can comprise silicon. In some cases, the pillars are disposed within a resin, e.g., an SU-8 resin. In another embodiment, the repeating structures can comprise a 3D arrangement of metal (e.g., silver) domains distributed with a polymeric crystal.

In another aspect, an integrated photonic device is disclosed, which comprises a substrate, a photonic crystal disposed on said substrate, where the photonic crystal exhibits a Dirac cone at the center of the Brillouin zone of its reciprocal lattice, e.g., at a frequency in the optical regime. An input waveguide is disposed on the substrate, where the input waveguide includes an input port for receiving radiation (e.g., from an external source or an internal source, such as a laser, incorporated within the device) and an output port optically coupled to the photonic crystal for transmitting at least a portion of said received radiation to the photonic crystal. The photonic device further includes an output waveguide that is disposed on the substrate, where the output waveguide has an input port for receiving at least a portion of the radiation exiting the photonic crystal. The output port of the output waveguide can be configured for optical coupling to a downstream component of the photonic device.

In some embodiments, the substrate can comprise silicon. Further, in some cases, a layer of silicon oxide can be disposed on a top surface of the substrate to electrically insulate the components of the photonic device from the substrate.

In some embodiments of the integrated photonic device, the photonic crystal comprises a 2D arrangement of pillars. In some embodiments, the pillars can be disposed in a resin. By way of example, the pillars can be formed of silicon and the resin can be a resin commonly known as SU-8.

In some embodiments of the photonic integrated circuit in which the photonic crystal comprises a 2D arrangement of pillars, the input waveguide is configured to transmit the radiation into the photonic crystal in plane of said pillars. Further, the output waveguide can be configured to receive the radiation through the photonic crystal in plane of the pillars.

Embodiments of in-plane, on-chip, integrated photonic devices according to the present teachings can provide many advantages, including, for example: 1) such a planar photonic device can allow for light to experience the negative/zero/positive index over a long distance, as it propagates in a plane parallel to the substrate, which increases the interaction length and allows the rich physics of negative/zero/positive index and Dirac-cone to be fully leveraged; 2) such an in-plane photonic device can be implemented in a variety of different shapes so as to explore the

abundant physics of negative/zero/positive index and Dirac-cone freely as well as to realize numerous on-chip devices; 3) such an integrated photonic device can be fabricated using standard planar processes over a large area with high fidelity; 4) such an in-plane photonic device can efficiently couple to optical waveguides to interface with standard integrated photonic circuits.

In another aspect, purely dielectric metamaterials are provided that exhibit a Dirac cone (or near Dirac-cone) at the center of the Brillouin zone of their reciprocal lattice, e.g., at a frequency in the optical regime. These metamaterials can provide many unique advantages: 1) they do not exhibit conduction losses because the structure is purely dielectric; 2) they exhibit low losses because the Dirac cone can be far away from the Mie resonance region; 3) the Dirac cone can provide simultaneously zero effective permittivity and permeability at a particular frequency. The simultaneous zero effective permittivity and permeability yields finite characteristic impedance, which can allow the metamaterial to provide good impedance-matching to free space and standard optical waveguides. In this manner, metamaterials exhibiting negative/zero/positive refractive index can be provided.

In a related aspect, methods of designing and fabricating Dirac-cone metamaterials demonstrating negative/zero/positive refractive index in the optical regime are provided. These metamaterials can exhibit exotic material properties and interesting physical phenomena, which can be employed in a variety of potential applications, such as electro-optic modulation, beam-steering, super-coupling, cloaking, surface-emitting lasers, phase-matching for nonlinear optics, rainbow-trapping, optical/quantum devices, energy sensing, biomedical sensing, and seismology.

Departing from well-established physical principles utilized conventionally for designing metamaterials, the present teachings provide in many embodiments negative/zero/positive refractive index metamaterials based on a Dirac cone at the center of the Brillouin zone of a photonic crystal, e.g., a purely dielectric photonic crystal. Some of the advantages of the present teachings are as follows:

Loss: in contrast to plasmonics and metallic resonators, many embodiments of the Dirac-cone metamaterials according to the present teachings do not involve any metallic constituents. This avoids parasitic metallic losses, especially in the optical regime. Also, as opposed to dielectric resonators, which usually achieve the negative/zero/positive refractive index around the Mie resonance (FIG. 1), Dirac-cone metamaterials can obtain negative/zero/positive refractive index far away from the Mie resonance. Considering that the effective constitutive parameters of a dielectric composite usually show a peak of loss around the Mie resonance and very low losses at any other frequency (FIG. 1), the negative/zero/positive refractive index provided by Dirac-cone metamaterials can be accompanied by a very low loss.

Impedance matching of zero-refractive-index: conventional metamaterials achieve zero-refractive-index by having either effective relative permittivity ϵ_r^{eff} or effective relative permeability μ_r^{eff} that is equal or near zero. This corresponds to an effective characteristic impedance η_{eff} of either infinity or zero, which results in impedance mismatch relative to free space and standard optical waveguides. On the other hand, because ϵ_r^{eff} and μ_r^{eff} of Dirac-cone metamaterials according to the present teachings can approach zero simultaneously and linearly at the Dirac point (FIG. 5a), the impedance η_{eff} of such a metamaterial has a finite value. This results in a good impedance match to free space and standard optical waveguides (*See*, e.g., FIG. 5d).

Feasibility in optical region: The metamaterials according to the present teachings can be fabricated so as to obtain the desired refractive index, e.g., at one or more wavelengths in a range of about 400 nm to about 1 cm, e.g., in a range of about 400 nm to about 100 μm. For example, as discussed in more detail below, in some embodiments, a (two-dimensional) 2D Dirac-cone metamaterial can include a 2D square array of silicon pillars, which is easy to fabricate using standard planar processes (*See*, e.g., FIG. 3).

Isotropy: Because the zero refractive index provided by Dirac-cone metamaterials is obtained at the Dirac point at the center of the Brillouin zone, it is isotropic. And, because the negative/positive refractive index of a Dirac-cone metamaterial is achieved in the vicinity of the Dirac point at the zone center, it is approximately isotropic.

Considering loss, impedance matching, feasibility and isotropy, the Dirac cone approach shows distinct advantages when compared with the well-established physical principles to achieve negative/zero/positive refractive index. By way of illustration, Table 1 below summarizes some of the advantages of the Dirac cone approach in accordance with the present teachings relative to conventional approaches employed for forming metamaterials:

Table 1

Physical principles	**Loss**	**Impedance matching of zero-refractive-index**	**Feasibility in optical regime**	**Isotropy**
Plasmonics	High	Poor	Good	Fair
Metallic resonators	High	Poor	Good	Poor
Periodically L-C loaded transmission lines	Low	Poor	Poor	Fair
Dielectric resonators	Medium	Poor	Poor	Good
Dirac cone	Low	Good	Good	Good

In some embodiments, by tuning the radius and pitch of a photonic crystal that includes an array of dielectric pillars, a Dirac-cone can be formed at the center of the Brillouin zone. The photonic crystal can be a square array, a triangular array, or any other two dimensional (2D) or three-dimensional (3D) photonic crystal. The dielectric materials of the pillars can be silicon, silicon nitride, or any other dielectric materials. In many embodiments, the pillars are formed using a dielectric material that exhibits a real dielectric constant contrast relative to a medium surrounding the pillars that is greater than about 1. Since the effective wavelength of the photonic crystal approaches infinity at the center of the Brillouin zone, the photonic crystal can

be treated as a homogeneous bulk metamaterial in the vicinity of the Dirac-point. The effective permittivity and permeability of the Dirac-cone metamaterials can approach zero simultaneously and linearly at the Dirac-point. Consequently, the effective impedance of such a metamaterial has a finite value, which provides good impedance matching to free-space and standard optical waveguides. Compared with other types of metamaterials, Dirac-cone metamaterials according to the present teachings have at least following advantages: 1) low loss; 2) good impedance matching to free space and standard optical waveguides; 3) feasibility of fabrication in optical regime.

As discussed in more detail below, a Dirac-cone metamaterial according to the present teachings can include silicon pillars disposed in an SU-8 resin matrix. In some embodiments, a metamaterial according to the present teachings can include a square array of silicon pillars disposed in an SU-8 matrix with gold mirrors disposed on top and bottom of the matrix. These structures can be formed as in-plane structures, which can provide at least the following benefits: 1) consistent unit cells; 2) ease of fabrication; 3) broad application in integrated on-chip optics.

The Dirac-cone metamaterials according to the present teachings can have a number of applications. For example, the zero-index of Dirac-cone metamaterials can be used to achieve phase-matching for nonlinear optics. In some embodiments in which a Dirac-cone metamaterial according to the present teachings is used as the propagation medium, the wave oscillations can cease in the metamaterial and all of the wavelets add up in-phase in all directions. By way of example, for four-wave mixing (inputs and output are at nearby wavelengths), a Dirac-cone metamaterial with a single Dirac-point, which shows zero index near the operating wavelength of the four-wave mixing, can be used. For second harmonic generation, where the input and output radiations are at quite different wavelengths, a Dirac-cone metamaterial with double Dirac-points, which shows zero-indices at the input and output wavelengths of the second harmonic generation, can be utilized.

Another application is for photonic crystal surface-emitting lasers (PCSELs). By replacing the quadratic-dispersion band edges of the regular PCSELs with the linear-dispersion bands provided by the Dirac-cone metamaterials, the mode spacing can be increased by order of

magnitude and the distributed in-plane feedback can be eliminated. It paves the way to achieve larger-area and higher-power single-mode PCSELs. In another application, the Dirac-cone metamaterials according to the present teachings can be used for electro-optic modulation. Because the existence of a Dirac cone at the center of the Brillouin zone is very sensitive to the refractive indices of the constituents, the existence of the Dirac cone can be controlled by tuning refractive indices of one or more constituents of the metamaterial, e.g., the refractive indices of the silicon and SU-8 using an applied electric field. When the Dirac cone exists, the metamaterial can show a pass-band around the Dirac point, otherwise, a bandgap opens up around the wavelength of the original Dirac point. If the operating wavelength of the incident light is around the Dirac point, the applied electric field determines whether or not incident light is transmitted through the modulator.

By way of example, such an amplitude modulator can be used for data transmission, where transmitted light corresponds to a '1' bit while no light corresponds to a '0' bit. Because the existence of a Dirac cone at the center of the Brillouin zone is very sensitive to the refractive indices of the constituents, such a modulator has the potential to achieve an ultralow drive voltage. Further, in some embodiments, such a modulator can achieve a device footprint as small as $3 \times 3\ \mu m^2$. In some embodiment, high electro-optic coefficient polymers can be employed to enhance the performance of such a modulator.

In another application, the metamaterials according to the present teachings can be employed to fabricate a zero-index coupler with in-phase outputs. By way of example, as discussed in more detail below, such a coupler can be designed by using a Dirac-cone metamaterial according to the present teachings as the waveguide and a 2D photonic bandgap structure as the side-wall. Such a coupler can operate around the wavelength of the Dirac-point to achieve zero-index. Such a coupler can have an arbitrary shape and can provide an in-phase output to all output channels.

In one aspect, a photonic structure is disclosed, which comprises a plurality of periodically repeating structures, said structures being configured and arranged relative to one another so as to form a photonic crystal exhibiting a Dirac cone at the center of the Brillouin

zone of its reciprocal lattice for at least one wavelength in the optical regime. In some embodiments, the Dirac cone is at a wavelength in a range of about 400 nm to about 100 μm. In some embodiments, such a photonic crystal can exhibit a band structure characterized by at least two substantially degenerate states having vanishing wavevectors.

In some embodiments, the repeating structures of the photonic crystal comprise a plurality of pillars. In some embodiments, the pillars have substantially cylindrical shapes with a radius of about 1/8 of said at least one wavelength, i.e., at the wavelength at which the photonic crystal exhibits the Dirac cone. Further, in some embodiments, the pillars can have a maximum height of about 1/3 of said at least one wavelength. In some embodiments, the pillars can have a height in a range of about 30% to about 60% of the wavelength at the Dirac cone or near Dirac-cone, e.g., at the operating wavelength.

In some embodiments, the pillars can exhibit a periodicity in each of two orthogonal dimensions in a plane perpendicular to their heights characterized by a lattice constant (a) such that a ratio of radius of said pillars to said lattice constant (r/a) is in a range of about 0.2 to about 0.3. In some embodiments, the diameter of the pillars is greater than about 100 nm.

In some embodiments, the pillars comprise a dielectric material exhibiting a real refractive index contrast relative to a material surrounding the pillars that is greater than about 1.

The pillars can be formed of a variety of different materials. By way of example, the pillars can comprise any of silicon, diamond, TiO_2, silicon nitride, aluminum oxide, InGaAsP, GaN, and InGaN.

In some embodiments, the pillars are disposed on a surface of an underlying dielectric substrate. The real refractive index of the material of which the substrate is formed is typically less than the real refractive index of the material of which the pillars are formed. By way of example, the dielectric substrate can comprises any of SiO_2, sapphire, InP, and polymeric resins, such as PDMS, Cytop, SU-8, and PMMA.

In some embodiments, a top metallic layer is disposed on top surfaces of said pillars. In addition, in some embodiments, a bottom metallic layer disposed on at least a portion of said surface of the dielectric substrate on which the pillar are disposed. In some embodiments, each of said top and bottom metallic layers has a thickness in a range of about 50 nm to about 100 nm. By way of example, the metallic layers can comprise any of gold and silver.

In some embodiments, the pillars can be sandwiched between two metallic layers. Such metallic layers can have a thickness in a range of about 50 nm to about 100 nm.

The photonic structure exhibits a substantially vanishing real refractive index at said at least one wavelength while concurrently exhibiting a non-zero real impedance at that wavelength. In some embodiments, the non-zero impedance exhibited by the photonic crystal can be tuned by adjusting the pitch and the radius of the pillars.

In some embodiments, the photonic structure exhibits a Q factor greater than about 20, and in some cases greater than about 1500, for at least two substantially degenerate states having a vanishing wavevector. Further, in some embodiments, the photonic crystal exhibits an imaginary refractive index less than about 0.1 at said at least one wavelength (i.e., at the wavelength at which the photonic crystal exhibits the Dirac cone).

In some embodiments, the pillars are disposed in a resin. By way of example, the resin can be any of SU8, Cytop, PMMA (polymethymethacrylate), and PDMS (polydimethylsiloxane).

In a related aspect, a photonic crystal is disposed, which comprises a plurality of periodically repeating structures, said structures being configured and arranged relative to one another so as to form a band structure providing at least two substantially degenerate states at the center of the Brillouin zone of a reciprocal lattice of the photonic crystal for at least one wavelength in the optical regime.

In another aspect, an integrated photonic device is disclosed, which comprises a substrate, a photonic crystal disposed on said substrate, said photonic crystal exhibiting a Dirac cone the

center of the Brillouin zone of its reciprocal lattice for at least one wavelength in the optical regime, an input port for receiving radiation and an output port optically coupled to said photonic crystal for transmitting at least a portion of said received radiation to said photonic crystal, and an output waveguide disposed on said substrate, said output waveguide having an input port for receiving at least a portion of the radiation transmitted through the photonic crystal.

In some embodiments, the output port of the output waveguide is configured for optical coupling to a downstream component of the photonic device.

In some embodiments of the integrated photonic device, the substrate comprises a dielectric substrate, such as silicon. In some embodiments, another dielectric substrate, such as silicon dioxide, sapphire, or InP, is disposed between a top surface of the substrate and the photonic crystal.

In some embodiments of the integrated photonic device, the pillars comprise any of silicon, diamond, TiO_2, silicon nitride, gallium arsenide, aluminum oxide, InGaAsP, GaN, and InGaN.

In some embodiments, the integrated photonic device further comprises a resin in which said pillars are disposed. The real refractive index contrast between the pillars and the resin can be greater than 1.

In some embodiments of the photonic crystal, the input waveguide is configured to transmit said radiation into the photonic crystal in plane of said pillars. In some such embodiments, the output waveguide is configured to receive the radiation transmitted through the photonic crystal in plane of said pillars.

In a related aspect, a photonic structure is disclosed, which comprise a plurality of periodically repeating structures, said structures being configured and arranged relative to one another so as to form a photonic crystal, where said photonic structure exhibits a substantially

vanishing real refractive index and a non-zero impedance for at least one wavelength in the optical regime.

In some embodiments, the periodically repeating structures comprise a plurality of pillars. In some such embodiments, the photonic structure exhibits a Q factor that is greater than 20, and in some cases greater than 1500, at said wavelength.

Further understanding of various aspect of the present teachings can be obtained by reference to the following detailed description in conjunction with the associated drawings, which are described briefly below.

Brief Description of the Drawings

FIG. 1 shows the effective relative permittivity as a function of frequency for a dielectric resonator;

FIG. 2 is a schematic diagram of a Dirac cone, showing a negative/zero/positive index of refraction;

FIG. 3 is a schematic diagram showing an embodiment of a Dirac-cone metamaterial according to an embodiment of the present invention;

FIG. 4A shows the formation of a Dirac cone at the center of the Brillouin zone;

FIG. 4B shows the effective relative permittivity ϵ_r^{eff} and effective relative permeability μ_r^{eff} for the structure corresponding to FIG. 4A;

FIG. 5A shows the real parts of ϵ_r^{eff} and μ_r^{eff} for the embodiment in FIG. 3;

FIG. 5B shows the imaginary parts of ϵ_r^{eff} and μ_r^{eff} for the embodiment in FIG. 3;

FIG. 5C shows the real and imaginary parts of n_{eff} for the embodiment in FIG. 3;

FIG. 5D shows the real and imaginary parts of the effective characteristic impedance η_{eff}, for the embodiment in FIG. 3;

FIG. 5E shows the phase velocity for the embodiment in FIG. 3;

FIG. 5F shows the group velocity for the embodiment in FIG. 3;

FIGS. 6A to 6E show various embodiments of Dirac-cone metamaterials according to various embodiments of the present invention;

FIG. 7 shows various steps in an exemplary method for fabricating the metamaterial structure shown in FIG. 6A, according to aspects of the present invention;

FIG. 8A shows scanning electron microscope (SEM) images of one embodiment of a metamaterial structure in four different fabrication stages according to aspects of the present invention;

FIG. 8B shows an optical image of an embodiment of a photonic chip including the metamaterial structure of FIG. 8A according to aspects of the present invention;

FIG. 8C shows an SEM image of the fabricated prism of FIG. 8A with silicon waveguide and SU-8 slab waveguide according to an embodiment of the present invention;

FIG. 8D shows an SEM image of the prism region for FIG. 8C, showing the path of a refracted beam;

FIGs. 9A-9D show various material parameters of the Dirac-cone metamaterial of FIG. 8A with optimized parameters according to aspects of the present invention;

FIGs. 10A-10D shows the finite-difference time-domain simulations and experimental results of the fabricated Dirac-cone metamaterial of FIG. 8A according to aspects of the present invention;

FIGs. 11A-11F shows the change in Dirac cone and extracted n_{eff} with different pillar radii according to aspects of the present invention;

FIGs. 12A and 12B show one example of a Mach-Zehnder interferometer (MZI) that can be employed to demonstrate a zero refractive index of a metamaterial according to aspects of the present invention;

FIGs. 13A and 13B show an electro-optic modulator having a 2D Dirac-cone metamaterial according to aspects of the present invention as well as frequency variations in ON and OFF states;

FIG. 14A-14C show simulations of out of plane electric field distribution for a metamaterial in a triangular array, showing negative, zero, and positive refractive indices according to aspects of the present invention;

FIGs. 15A and 15B show simulations of out-of-plane electric field distribution in a 90 bending channel in which the channel is filled with air and a 2D Dirac-cone metamaterial respectively;

FIG. 16 shows one embodiment of Dirac-cone metamaterials used for rainbow trapping according to aspects of the present invention;

FIG. 17 is a unit cell of a 3D Dirac-cone metamaterial according to aspects of the present invention;

FIGs. 18A-18F show schematics of various embodiments of ZIM structures including LLZIM and AD-ZIM, and their representative *xy* mode distributions in single unit cell forming PDC at Γ point according to aspects of the present invention;

FIG. 19A is a schematic model of a unit cell with a PEC boundary at the top of the SU-8 layer;

FIG. 19B shows simulated Q and λ as a function of h_{SU-8} for the model in FIG. 19A;

FIG. 19C is a schematic model of a unit cell with a realistic gold mirror having h_{Au} = 100 nm;

FIG. 19D shows simulated Q and λ as a function of h_{SU-8} for the model in FIG. 19C;

FIGs. 20A-20C show schematics illustrating optimization of one embodiment of an LLZIM according to the present teachings;

FIGs. 21A-21C show structural parameters for LLZIM optimization for one embodiment according to aspects of the present invention;

FIGs. 22A-22C show matching Dirac-point and high Q by applying the parameters in FIG. 21C, and simulated band structure around the Γ point with optimal parameters according to aspects of the present invention;

FIG. 23 shows simulated 3D dispersion surfaces of a PDC for an LLZIM with the same parameters as FIG. 22C according to aspects of the present invention;

FIGs. 24A-24C show robustness of a ZIM having a double mirror and robustness of an AD-ZIM respectively, and simulated band structures around the Γ point for the AD-ZIM according to aspects of the present invention;

FIG. 25 shows simulated 3D dispersion surfaces of an AD-ZIM according to aspects of the present invention;

FIGs. 26A-26B show verification of the relationship between n_{eq} and $\Delta\lambda/\Delta r$ according to aspects of the present invention;

FIGs. 27A-27D show structural dependences of various modal parameters in an ADZIM according to aspects of the present invention;

FIGs. 28A-28E show optimized robustness derived from the slopes in FIGs. 27A-27D and tuning with the scaling law according to aspects of the present invention;

FIGs. 29A-29C show optical microscope images of one of embodiment of a fabricated on-chip AD-ZIM prism device according to aspects of the present invention; and

FIGs. 30A-30D show characterization of one embodiment of a super-robust AD-ZIM, including SEM images of a fabricated device according to aspects of the present invention.

Detailed Description

The present teachings relate generally to designing and fabricating optical metamaterials with negative/zero/positive refractive index based on a novel physical principle in photonics: a Dirac cone at the center of the Brillouin zone. It is a photonic analog of the gapless dispersion of graphene in the center of the Brillouin zone. In many embodiments of the present teachings, the metamaterials include purely dielectric constituents, and hence do not exhibit conduction losses. Furthermore, because in many embodiments the Dirac cone is far away from the Mie-resonance region, around which a peak of loss appears, the metamaterials according to the present teachings will show negative/zero/positive refractive index with an extremely low loss, e.g., characterized by an imaginary index of 0.03 or even 0.003. Also, as opposed to the zero-refractive-index provided by either permittivity or permeability near zero metamaterials, the metamaterials according to many embodiments of the present teachings can achieve zero-refractive-index at a particular frequency in the optical regime with both permittivity and permeability simultaneously zero. This double-zero property results in finite characteristic impedance. In contrast, the impedance exhibited by conventional metamaterials, which exhibit near zero permittivity (permeability), can be infinite or zero, thereby leading to significant impedance mismatch. Thus, the metamaterials according to the present teachings exhibiting zero-refractive-index overcome a big drawback of traditional single zero metamaterials.

As discussed in more detail below, in some embodiments, two dimensional (2D) Dirac-cone metamaterials according to the present teachings can be implemented by a 2D square array of silicon pillars, which can be fabricated by top-down methods. The negative/zero/positive refractive index of metamaterials according to the present teachings, such as the 2D embodiments, can be characterized by multiple methods, such as a prism-based method and an

interferometry-based method. The negative/zero/positive refractive index metamaterials according to the present teachings with super low losses and good impedance matching can be used to demonstrate a number of interesting physical phenomena and can be employed in a number of potential applications, such as electro-optic modulation, beam-steering, super-coupling, cloaking, surface-emitting lasers, phase-matching for nonlinear optics, and rainbow-trapping. Furthermore, such potential applications can be pursued in optical/quantum devices, energy sensing, biomedical sensing, and seismology.

A photonic crystal can be treated as a homogeneous bulk metamaterial in the vicinity of the Dirac point because the homogenization criterion (effective wavelength λ_{eff} inside a medium is much larger than the lattice constant) is met (basically, $\lambda_{\text{eff}} \to \infty$ at the Dirac point Γ as shown in FIG. 2). Such a photonic crystal can exhibit the following characteristics: 1) in the vicinity below the Dirac point, the fact that group velocity and phase velocity have opposite directions (backward wave) implies a negative refractive index ($n_{\text{eff}} < 0$), as illustrated in FIG. 2; 2) at the Dirac point Γ, $k = 0$ results in $n_{\text{eff}} = k/\omega = 0$, as illustrated in FIG. 2; and 3) in the vicinity above the Dirac point, the fact that group velocity and phase velocity have the same directions (forward wave) induces positive refractive index ($n_{\text{eff}} > 0$), as illustrated in FIG. 2. However, the Dirac cone usually appears at the zone boundary for many conventional photonic crystals, which cannot meet the homogeneous criteria. By carefully choosing the geometry and material parameters of a photonic crystal according to the present teachings, a Dirac cone can be formed at the zone center due to the accidental degeneracy, in which, for the 2D case, one monopole eigenstate and two double-degenerate dipole eigenstates have the same eigenfrequency. Although the Dirac cone at the zone center is actually a "Dirac-like cone" because its corresponding linear dispersions possess zero Berry phase and cannot be mapped into the massless Dirac Hamiltonian, it still can imply a homogeneous metamaterial with negative/zero/positive n_{eff}, as discussed previously. Furthermore, it has been proven that the presence of a Dirac cone at the zone center is only determined by the spatial symmetry of two modes rather than the detail of the 2D/3D photonic structure, which leads to a great degree of freedom to design a Dirac-cone metamaterial in view of the available fabrication and characterization techniques.

In the following discussion, the center of a Brillouin zone of a reciprocal lattice (also known as the Γ point) of a photonic crystal refers to a point in the Brillouin zone that corresponds to a vanishing wavevector, i.e., **k**= 0. In the case of a two-dimensional photonic crystal, the center of the Brillouin zone is characterized by a wavevector having $k_x = 0$ and $k_y=0$, where the photonic crystal exhibits periodicity in the x-y plane.

The term "optical regime" as used herein refers to a portion of the electromagnetic spectrum corresponding to vacuum wavelengths in a range of about 400 nm (nanometer) to about 1 cm (centimeter), e.g., in a range of about 400 nm to about 100 μm, or in a range of about 100 nm to about 25 μm.

The term "substantially degenerate" as used herein refer to at least two Block states of a photonic crystal that are characterized by **k**= 0 and difference in frequency (i.e., a band gap) that is equal to or less than 3% of the center frequency between the two states. As discussed in more detail below, such substantial degeneracy can be achieved in some embodiments by a band structure exhibiting a near Dirac cone at **k**= 0.

The term "near Dirac-cone" as used herein refers to having a wavelength difference between to states, which would be degenerate in case of a perfect Dirac-cone, of equal to or less than 3% of the operation frequency, i.e., 3% of the Dirac-cone wavelength.

The term "about" for modifying numerical values as used herein indicates a maximum variation of +/- 5%.

FIG. 3 schematically depicts an embodiment of a Dirac-cone metamaterial according to the present teachings, which includes a 2D square array 300 of silicon pillars 302 with parameters $a = 856.1$ nm, where a is the period of the array, and pillar radius $r = 170.6$ nm at 1.55 μm. This structure can be readily fabricated by electron-beam (e-beam) lithography and ICP-RIE dry etching. The chosen values of the radius and the period of the array results in the formation of a Dirac cone at the center of the Brillouin zone (FIG. 4A). The effective relative permittivity ϵ_r^{eff} and effective relative permeability μ_r^{eff} of this structure were calculated using an

effective medium theory, which is still valid beyond the homogenization criterion ($k_{\text{eff}}a < 1$)). As shown in FIG. 4B, the $\epsilon_{\text{r}}^{\text{eff}}$ and $\mu_{\text{r}}^{\text{eff}}$ indeed show double-negative behavior below the Dirac point, double-zero at the Dirac point, and double-positive above the Dirac point, as mentioned before.

To further investigate the fundamental optical properties of 2D Dirac-cone metamaterials, complex $\epsilon_{\text{r}}^{\text{eff}}$, $\mu_{\text{r}}^{\text{eff}}$, n_{eff}, and effective characteristic impedance η_{eff}, as well as the phase velocity v_{p} and group velocity v_{g} of the above 2D array of silicon pillars shown in FIG. 3 were calculated. The v_{p} and v_{g} were calculated using their original definitions: $v_{\text{p}} = \omega/k$ and $v_{\text{g}} = c/[n_{\text{eff}} + \omega(\partial n_{\text{eff}}/\partial\omega)]$. The parameters of this metamaterial were chosen as follows: $a = 856.1$ nm and $r = 170.6$ nm (Figure 3) to make $\epsilon_{\text{r}}^{\text{eff}}$ and $\mu_{\text{r}}^{\text{eff}}$ perfectly intersect at zero at 1.55 μm.

As shown in Figures 5A and 5B, the real parts of $\epsilon_{\text{r}}^{\text{eff}}$ and $\mu_{\text{r}}^{\text{eff}}$ show double-negative, double-zero, and double-positive behaviors in the vicinity of the Dirac point while their imaginary parts are almost zero around the Dirac-point region. Furthermore, as shown in FIG. 5C, the real parts of n_{eff} show negative, zero, and positive values corresponding to the double-negative, double-zero, and double-positive behaviors of $\epsilon_{\text{r}}^{\text{eff}}$ and $\mu_{\text{r}}^{\text{eff}}$. Similarly, the imaginary parts of n_{eff} are close to zero around the Dirac-point region. Hence, this 2D Dirac-cone metamaterial can show negative/zero/positive n_{eff} with an extremely low loss. As shown in FIG. 5D, η_{eff} has a value of 1.7 around the Dirac-point region, which results in a reflection coefficient of about 26% relative to free space. Thus, this 2D Dirac-cone metamaterial can provide a good impedance matching to free space and a variety of waveguide structures. As shown in Figures 5E and 5F, v_{p} has a singularity at the Dirac point while v_{g} is smaller than the vacuum light speed around the Dirac-point region. This slow light behavior can have potential applications in optical/quantum devices. Also note that the signs (directions) of v_{p} and v_{g} in the vicinity of Dirac point are in good agreement with those predicted in FIG. 2.

In some embodiments, the Dirac-cone metamaterials according to the present teachings are capable of effectively confining the light that enters the metamaterials. By way of example,

FIG. 6A shows schematically an embodiment that includes a 2D array of silicon pillars 600 disposed on an underlying top surface of an SiO_2 layer 608 and within an SU-8 resin 602, e.g., the 2D arrangement of silicon pillars discussed above in connection with FIG. 3. An upper metallic, e.g., gold, layer 604 is disposed on top of the pillars and a lower metallic, e.g. gold, layer 606 is disposed on the top surface of the SiO_2 layer between the pillars. The underlying SiO_2 layer 608 is turn disposed on a silicon substrate 610. The metallic layers provide confinement of the light coupled into the region of the metamaterial in which the silicon pillars are disposed. This structure has the advantage of ease of fabrication. However, in some embodiments, the gold layers can introduce absorption losses. To reduce these losses, FIG. 6B schematically depicts another embodiment of a metamaterial according to the present teachings in which the gold layers are replaced with a pair of distributed Bragg reflectors (DBRs). More specifically, this embodiment includes a 2D array of silicon pillars 600 disposed in an SU-8 resin 602, e.g., the arrangement of 2D silicon pillars shown in FIG. 3, where resin, including the silicon pillars, is sandwiched between a pair of distributed Bragg reflectors 612. The DBRs provide confinement of radiation coupled into the region where the silicon pillars are disposed.

By way of another example, FIG. 6C depicts another embodiment of a metamaterial according to the present teachings, which includes a 2D array of silicon pillars 600 disposed in a resin 602 (e.g. SU-8 resin), e.g., the arrangement of the silicon pillars shown in FIG. 3, that is sandwiched between a lower metal layer (e.g., a gold layer) 606 and an upper distributed Brag reflector (DBR) 612. This hybrid structure can have the advantage of low loss and fabrication simplicity.

To further confine the light in the region in which the 2D array of pillars are disposed, FIG. 6D schematically depicts a metamaterial according to an embodiment of the present teachings, which includes in addition to an upper and a lower metallic layers 604 and 606, two metal (e.g., gold) lateral layers 614 and 616 that provide lateral mirrors for lateral confinement of the light. Similar to the embodiment shown in FIG. 6A, the lower metallic layer is disposed on an underlying SiO_2 layer 608, which is in turn disposed on a silicon substrate 610. By way of another example, FIG. 6E schematically depicts another embodiment of a metamaterial according to the present teachings, which includes a 2D array of pillars 600 disposed in a resin,

e.g., the arrangement of silicon pillars shown in FIG. 3 above, and further includes a lower and an upper metal (e.g., gold) layers 604 and 606 that provide longitudinal (i.e., along a dimension parallel to the length of the pillars) light confinement. In addition, the exemplary metamaterial shown in FIG. 6E includes a pair of 2D photonic bandgap (PBG) structures 618 and 620 that function as lateral mirrors to provide transverse (i.e., along a dimension perpendicular to the length of the pillars) light confinement.

FIG. 7 shows various steps in an exemplary method for fabricating an implementation of the metamaterial structure shown in FIG. 6A in which a plurality of silicon pillars is disposed on a surface of an underlying substrate with a lower gold layer disposed on the substrate surface and a top gold layer disposed on the top of the pillars.

In an initial step (1), an SOI (silicon-on-insulator) wafer (500nm Si on 3000 nm SiO_2) is spin-coated with a negative tone resist (e.g., HSQ) 700. The waveguides and the pillars are patterned using e-beam lithography in the same step. An ICP-RIE dry etching is employed to form the waveguide 702 and pillar structures 704 (step 2), using the negative resist (e.g., HSQ) as a mask. In a wet etch step (3), the previous resist (HSQ) mask is removed. The sample is then spin-coated with a positive tone resist (PMMA) 706. The sample is patterned again using e-beam lithography, this time leaving gaps for where the metal layer (e.g., gold layer) would be. A layer of a metal (e.g., gold) is deposited using e-beam evaporation (step 4). Then a lift-off step is performed, leaving a layer 708 of metal (e.g., gold) at the base of the pillars. This serves as one of the mirrors of the waveguide. Another negative-tone resist 710, e.g., SU-8, is spin-coated (step 5). This resist will remain as part of the device and serves multiple roles: within the zero-index medium, it also supports the top layer of gold, and it can also be used as an off-chip coupler to help facilitate coupling into the waveguides (at the facet). These patterns can be written using e-beam lithography. In subsequent step (6), which is similar to step 3, PMMA 712 can be spin-coated and patterned using e-beam lithography, leaving a gap for subsequent gold deposition. In step (7), similar to step (4), a layer of a metal (e.g., gold) can be deposited using e-beam evaporation and lift-off, leaving a layer 714 of metal (e.g., gold) on the top of the pillars, serving as the second mirror. The gold layers can be extended, if desired, beyond the zero index pillar structure in order to wire-bond and tune the properties of the material. In step (8), similar

to step (5), the SU-8 fiber coupler and output waveguide 716 are patterned using e-beam lithography.

By way of illustration, FIG. 8A shows scanning electron microscope (SEM) images of a metamaterial structure according to an embodiment of the present teachings in four different fabrication stages: I. Silicon pillars on a silicon-on-insulator (SOI) substrate; II. Silicon pillars with bottom gold layer; III. Silicon pillars in SU-8 matrix with bottom gold layer; IV. Silicon pillars in SU-8 matrix with top and bottom gold layers (completed structure). Inset of FIG. 8A shows a schematic three-dimensional view of one unit-cell of the metamaterial. The period and radius of the silicon pillars are $a = 690$ nm and radius $r = 211$ nm, respectively. The height of silicon pillars is $h_{\mathrm{Si}} = 512$ nm, the SU-8 layer thickness is $h_{\mathrm{SU-8}} = 595$ nm, and gold layer thickness is $h_{\mathrm{Au}} = 50$ nm.

Photonic crystals according to the present teachings can be employed to form a variety of photonic devices. By way of example, FIG. 8B shows an optical image of a photonic chip showing fiber couplers 800, spot-size converters 802, waveguides 804, and a Dirac-cone photonic crystal according to an embodiment of the present teachings with the pillars arranged in the form of prisms 806 corresponding to the metamaterial structure of FIG. 8A. FIG. 8C shows an SEM image of the fabricated prism 810 of FIG. 8A with silicon waveguide 812 and SU-8 slab waveguide 814. Inset of FIG. 8C schematically shows the prism 810, which is a right triangular array of pillars 816 measuring 8 unit cells across, without gold and SU-8 layers. FIG. 8D shows an SEM image of the prism region showing the path of a refracted beam 818 (also shown in FIG. 8C). The angle of refraction α is determined by measuring the position of the refracted beam at the curved output edge of SU-8 slab waveguide (shown as spot 820 in FIG. 8C).

FIGs. 9A-9D show calculated material properties of the Dirac-cone metamaterial of FIG. 8A with optimized parameters. FIG. 9A shows the photonic band structure of the 3D Dirac-cone metamaterial of Fig. 8A for TM mode. Two linear dispersion bands intersect at the Γ point at $\lambda = 1590$ nm, forming a Dirac-like cone. FIG. 9B shows 3D dispersion surfaces near the Dirac-point wavelength. The linear bands 900 and 902 form the cones, which meet at the Dirac point. The quadratic band 904 crossing the Dirac point is a quasi-longitudinal mode. FIG. 9C shows the

effective relative permittivity and permeability of the metamaterial retrieved from numerically calculated reflection and transmission coefficients. Inset of FIG. 9C shows the electric and magnetic fields in a unit-cell at the Dirac-point wavelength, depicting an electric monopole and a transverse magnetic dipole behavior. FIG. 9D shows isofrequency contours of the Dirac-cone metamaterial. The nearly circular contours indicate that the index is nearly isotropic near the Γ point.

As discussed further below, it should be understood that photonic crystals fabricated based on the present teachings may exhibit a slight lifting of the degeneracy at the center of the Brillouin zone due to fabrication imperfections. Such lifting of the degeneracy can be equal to or less than about 3% of the central frequency of the band gap (in other words, 3% of the frequency of a Dirac-cone at the center of the Brillouin zone in absence of the lifting of the degeneracy). For example, such lifting of the degeneracy can be less than about 6 THz.

FIGs. 10A-10D show the finite-difference time-domain simulation and experimental results of the fabricated Dirac-cone metamaterial of FIG. 8A. FIG. 10A (left) illustrates the simulated out-of-plane electric field in the prism and SU-8 slab waveguide region of Fig. 8A, showing that the two first order diffraction beams are on both sides ($\pm 70^{o}$) of the zero-order (refracted) beam, which is normal to the interface between prism and SU-8 slab waveguide. FIG. 10A (right) shows field distribution in the prism region at 1570 nm, illustrating the nearly constant spatial phase distribution within the prism. FIG. 10B illustrates the near-infrared microscope image of the prism and SU-8 slab waveguide region at 1570 nm. The zero-order (refracted) beam and its first order diffraction beam are visible at the curved output edge of SU-8 slab waveguide at 0^{o} and -70^{o}, respectively. FIG. 10C shows simulated (left) and measured (right) far-field patterns. The white dashed line indicates the wavelength, 1570 nm, at which the refracted beam crosses 0^{o}. The image intensity has been normalized at each wavelength for clarity. FIG. 10D shows measured and simulated effective index of the Dirac-cone metamaterial. The dots indicate the measured refractive index, with error bars representing the uncertainties in the measurement. The measurement agrees well with the simulated effective index (solid line).

Theoretically, a photonic Dirac-cone has no bandgap at the Dirac-point wavelength. In some embodiments, the photonic Dirac-cone metamaterial may have no bandgap at the Dirac point wavelength. In other embodiments, due to fabrication imperfections, however, a tiny bandgap may open near the targeted Dirac-point wavelength of an experimentally fabricated Dirac-cone metamaterial. In this bandgap, the real index has a constant zero value. Given the error bars shown in Fig. 10D, the measured bandgap is at most 49 nm, centered at 1555.5 nm. To further confirm the fact that the measured zero index is induced by a Dirac-cone instead of a bandgap, the properties of two metamaterial structures in the form of two prisms with slightly smaller and larger pillar radii were simulated. FIGs. 11A-11F show the change in Dirac cone and extracted n_{eff} with different pillar radii. FIG. 11A, FIG. 11C, and FIG. 11E illustrate the simulated band structures of metamaterials with $r = 167.5,\ 190,$ and 210.5 nm, respectively. The electric monopole mode is indicated by dots forming the curves 1100, and the transverse magnetic dipole modes are indicated by dots forming the curves 1102. Insets show E_z profiles corresponding to each band at the Γ point. FIG. 11B, FIG. 11D, and FIG. 11F show the effective indices n_{eff} extracted from refractions through prisms with $r = 167.5,\ 190,$ and 210.5 nm, respectively. Simulations are shown by solid curves, and measured results are shown by dots with error bars. These results show that bandgaps of the prisms with smaller and larger radius become much wider and blue shifted and red shifted, respectively. This behavior is consistent with theoretical predictions.

FIGs. 12A and 12B show schematically a Mach-Zehnder interferometer (MZI) that can be employed to demonstrate a zero refractive index of a metamaterial according to some embodiments of the present teachings. More specifically, FIG. 12A shows an asymmetric MZI without a zero-refractive-index arm, which can show intensity modulation as the length of that arm varies. FIG. 12B in turn shows an asymmetric MZI in which the non-reference arm includes a metamaterial 1200 exhibiting a zero refractive index according to embodiments disclosed herein. A change in the length of such a metamaterial does not result in observation of an intensity modulation since the phase difference between the two arms depends solely on the total phase that light has acquired while propagating in the metamaterial.

Applicants have discovered, via theoretical analysis of Dirac-cone metamaterials, that the

existence of a Dirac cone at the center of the Brillouin zone of a metamaterial according to the present teachings can be sensitive to the variations in the geometry and material parameters of the constituents of the metamaterial. These variations can arise, e.g., from achievable tolerances in the fabrication process. To compensate for the fabrication tolerances so as to obtain the designed Dirac cone, in some embodiments, the following tunability methods can be employed. In one method, the refractive indices of the pillars and/or the material surrounding the pillars (e.g., silicon pillars and SU-8 in the embodiment of the FIG. 6A) can be adjusted (tuned) based on the electro-optic effect. By way of example, this tunability can be obtained by applying voltage to the gold thin films, which are used as electrodes, as shown, e.g., in FIGs. 6A and 7 (step 8). In another method, the geometric and material parameters of the constituents of the metamaterial can be tuned by adjusting the temperature. By way of example, in some embodiments, the metamaterial can be coupled to a temperature-controlling module, such as a Peltier thermoelectric cooler. In some cases, the temperature of a photonic crystal according to the present teachings can be adjusted to compensate for a lifting of degeneracy at $\mathbf{k}=0$, which may have occurred due to fabrication imperfections.

The metamaterials according to the present teachings can exhibit interesting physical phenomena and can be employed in a variety of applications. By way of example, such metamaterials can be employed in electro-optic modulators. Based on the fact that electro-optically active materials have a birefringence that is proportional to the electric field, the electro-optic effect can be used to generate both amplitude and phase modulation of optical beams. The fundamental scheme of both kinds of modulation is that the refractive index of an electro-optically active material can be different along two axes perpendicular to the direction of light propagation. Typically, three criteria can be employed to evaluate the performance of an optical modulator: 1) drive voltage, which should be as low as possible; 2) modulation speed; 3) device footprint. In recent years, many crystal and silicon based electro-optic modulators have been proposed and have achieved good performance.

By way of example, FIG. 13A schematically depicts an electro-optic modulator according to an aspect of the present teachings, which is based on 2D Dirac-cone metamaterials disclosed in the present teachings. The exemplary electro-optic modulator is in the form of an

integrated photonic device 1300, which includes a metamaterial comprising a 2D array of pillars 1302, e.g., the 2D arrangement of silicon pillars shown in FIG. 3, within an SU-8 matrix 1304. An input waveguide 1306 allows coupling input radiation 1308 into the metamaterial and an output waveguide 1310 receives the radiation 1312 exiting the metamaterial. The input waveguide 1308 couples the radiation into the metamaterial in plane of the array i.e., the pointing vector of the radiation is perpendicular to the length of the pillars. The input and output waveguides 1306 and 1310 and the metamaterial are disposed on an underlying substrate 1314, e.g., a silicon substrate coated with a layer of SiO_2 1316, to form an integrated photonic device. Two metal pads 1318 and 1320 allow the application of a voltage across the metamaterial.

Because the existence of a Dirac cone at the center of the Brillouin zone can be very sensitive to the refractive indices of the constituents of the metamaterial. In some embodiments the existence of Dirac cone can be tuned by modulating the refractive indices of the silicon and SU-8 using an applied electric field. When the Dirac cone exists, the metamaterial shows a pass-band around the Dirac point, as shown in FIG. 13B, otherwise, a bandgap opens up around the wavelength of the original Dirac point, as shown in FIG. 13C. If the operating wavelength of the incident light is around the Dirac point, as shown by the gray regions in Figures 13B and 13C, the applied electric field determines whether or not incident light is transmitted through the modulator.

By way of example, such an amplitude modulator can be used for data transmission, where transmitted light corresponds to a '1' bit while no light corresponds to a '0' bit. Because the existence of a Dirac cone at the center of the Brillouin zone is very sensitive to the refractive indices of the constituents, the proposed modulator has the potential to achieve an ultralow drive voltage. In some embodiments, the electro-optic modulator can achieve a device footprint as small as $3.3 \times 3.3\ \mu m^2$. To further improve the performance, high electro-optic coefficient polymers and shorter pillars can be employed.

In some embodiments, input laser light can be coupled into the above electro-optic modulator at proper wavelengths using lensed-fiber coupling. Then, the transmission levels of radiation through the electro-optic modulator can be observed for different biases. These results

can then be utilized to find the operating points of the modulator. In some cases, the electro-optic modulator can be employed to modulate light using, for example, high-speed pseudo random binary signal generator, RF amplifier, O/E converter, and sampling oscilloscope. In some cases, an error detector can be used to evaluate the bit error.

In another embodiment, an on-chip beam-steering device that employs metamaterials according to the present teachings is disclosed. Although mechanical beam-steering has been widely used in sensing and imaging, conventional beam steering systems have limitations with regard to the speed and size of the system. An on-chip beam-steering device has a broad range of applications, such as laser printers and chip-to-chip optical communications. There are typically two criteria for evaluating the performance of a beam-steering technique: 1) the maximum beam-steering angle $\theta_{\mathrm{r-max}}$, which has to be much larger than the beam divergence angle θ_{div}; 2) the number of pixels that can be created in the far-field has to be larger than 1,000 to meet the requirement of practical applications.

In some embodiments, beam-steering can be achieved by sweeping the operating wavelength of an input light around the Dirac point of a triangular-prism-shaped 2D Dirac-cone metamaterial in accordance with the present teachings (*See* for example FIGs. 14A-14C). Because this metamaterial can show a negative/zero/positive refractive index in the vicinity of the Dirac point, this method has the potential to yield a large $\theta_{\mathrm{r-max}}$. In some embodiments, the beam-steering angles at diffierent operating wavelengths can be measured using an optical camera. The number of pixels can then be calculated using, e.g., $\theta_{\mathrm{r-max}}/\theta_{\mathrm{div}}$.

FIGs. 14A to 14C show FDTD simulations of a theoretical metamaterial based on the structure of FIG. 3 with the following parameters for the 2D array of pillars: $a = 658$ nm and $r = 170$ nm. The metamaterial has the form of a triangular prism. The refractive index of the metamaterial around 1.55 μm can be determined by calculating the refraction angle of the light propagating through the prism by Snell's law. This provides a straightforward and unambiguous determination of the refractive index because the refraction angle depends only on the phase gradient that the light beam experiences when refracted from the angled output face of the prism. This is illustrated in FIGs. 14A to 14C by FDTD simulations of the out-of-plane electric fields

distribution in the prism at 1.4 μm, 1.55 μm, and 1.7 μm, in which the metamaterial shows negative, zero, and positive refractive indices, respectively.

More specifically, FIG. 14A shows the phase-front of light at 1.4 μm, indicating positive refraction angle (positive-phase propagation) resulting from a positive refractive index. FIG. 14B shows zero refraction angle (zero phase propagation) due to a zero refractive index, and FIG. 14C shows a negative refraction angle (negative-phase propagation) resulting from a negative refractive index.

Another application of metamaterials according to the present teachings relates to super coupling. By using a channel that is filled with zero-refractive-index to connect two waveguides, the light can be efficiently transferred between these two waveguides regardless of the channel's shape and length. This phenomenon has three attractive features: 1) the light intensity is enhanced inside the narrow channel since the energy has to squeeze through this narrow channel without reflection; 2) the enhanced intensity keeps a uniform phase inside the channel due to fact that the wavelength in a zero-refractive-index metamaterial is infinitely long; and 3) this enhancement with its uniform phase inside the channel is independent of the shape and length of the channel. The potential applications of this phenomenon include: 1) boosting nonlinear effects and second-harmonic generation; 2) enhancing the photon density of state for emitters inside the zero-refractive-index structures; 3) sensing a defect inside the channel. By using the zero-refractive-index provided by a Dirac-cone metamaterial according to the present teachings for super-coupling, at least the following two advantages can be obtained when compared with using metallic, epsilon-near-zero metamaterials: 1) less energy losses along the channel because of the low-losses of the zero-refractive-index material; 2) less reflection at the boundary between waveguide and channel due to the fact that this zero-refractive-index is associated with a finite characteristic impedance.

For example, a waveguide coupling structure according to some embodiments can include a 2D square array of silicon pillars. An example of such a structure is shown in FIG. 15, which includes gold layers as the top, bottom, and lateral walls of the waveguide (*See* FIG. 6 and the associated description for more details regarding this structure). As shown in FIG. 15A, electromagnetic waves can travel with little distortion through a waveguide that is filled with a

Dirac-cone material according to the present teachings. More specifically, FIG. 15B is an FDTD simulation of out-of-plane electric field distribution in a 90-degree bending channel in which the channel is filled with a 2D Dirac-cone metamaterial according to an embodiment of the present teachings. The excitation at the bottom-right is plane wave and the boundaries of the channel are formed by gold. As a control, FIG. 15A shows simulation of out-of-plane electric field distribution in a 90-degree bending channel in a beam-steering system in which the channel is filled with air. The simulation shows that when the metamaterial is replaced with air, the incident waves are mostly reflected backwards by the 90 bending channel wall without super-coupling effect. In some embodiments, the performance of a waveguide coupling structure utilizing a Dirac-cone metamaterial according to the present teachings can be characterized by using the method similar to the one discussed above in connection with the electro-optic modulator.

Dirac-cone metamaterials according to the present teachings can have other applications. An axially varying heterostructure with a negative-refractive-index core can efficiently and coherently bring light to a complete standstill. Each wavelength component of the wave packet is stopped at a different core thickness, giving the spatial distribution of the spectrum and forming the "trapped rainbow" phenomenon. Compared with other methods of achieving slow light, this scheme has the advantages of broadband, high in-coupling efficiencies, and room temperature operation. Rainbow-trapping has been previously realized using tapered metamaterial waveguides with metallic structures.

In some embodiments, a negative-refractive-index Dirac-cone metamaterial according to the present teachings can be used as the core of a tapered waveguide to trap a rainbow. Compared with conventional methods, the use of negative-refractive-index Dirac-cone metamaterials according to the present teachings has the advantage of low-losses along the tapered waveguide.

More specifically, in some embodiments, a 2D Dirac-cone metamaterial with gradient geometric parameters can be utilized to achieve a negative-refractive-index over a broadband along the core of a tapered waveguide. In some embodiments, Dirac-cone metamaterials can be

designed in accordance with the present teachings using effective-medium theory such that each metamaterial exhibits a negative-refractive-index at one of a plurality of different wavelengths. Then, the metamaterials can be arranged within the core of a tapered waveguide to achieve a particular value of negative-refractive-index at different core thicknesses corresponding to different operating wavelengths. The parameters of the entire waveguide can then be optimized using FDTD simulation. By way of example, the performance of such a tapered waveguide can be characterized by using an optical microscope to image the light propagation through the tapered waveguide from the open side of the waveguide.

By way of further illustration, FIG. 16 schematically shows the use of Dirac-cone metamaterials according to the present teachings for rainbow trapping. The arrow indicates wave propagation direction. The media I, II, and III are three homogeneous and isotropic materials with respective refractive indices: $n_{\mathrm{I}} > n_{\mathrm{II}} > n_{\mathrm{III}}$. A tapered waveguide include metamaterials according to the present teachings in the manner discussed above. A guided wave can propagate from a conventional waveguide formed of medium I to the negative-refractive-index medium, in which it propagates smoothly due to the slow reduction in the thickness of the waveguide core. The smaller wavelength components of the wave are trapped at the larger core thickness (left), while the larger components are trapped at the smaller core thickness (right).

In another aspect, the present teachings provide 3-dimensional (3D) Dirac-cone metamaterials. The presence of a Dirac cone at the zone center is only determined by the spatial symmetry of two modes rather than the detail of the 2D/3D photonic structure. This provides the freedom to design a 3D Dirac-cone metamaterial using available fabrication and characterization techniques. In some embodiments, a cubic array of silver spheres or silver unit-cell with regular cube symmetry can be employed to form a 3D metamaterial according to the present teachings. In some embodiments, a 3D structure can be designed theoretically and optimized using, e.g. FDTD simulation taking into account the fabrication tolerance and material properties. By way of illustration, FIG. 17 schematically shows a unit cell of a 3D Dirac-cone metamaterial according to an embodiment of the present teachings, incorporating repeating patterns of silver.

In some embodiments, femtosecond laser direct-writing methods, such as those disclosed

in published international patent application PCT/US2012/022036 entitled "Micro-and nano-fabrication of connected and disconnected metallic structures in three-dimensions using ultrafast laser pulses" (WO 2012100167), and articles entitled "Fabrication of disconnected three-dimensional silver nanostructures in a polymer matrix," published in Applied Physics Letters, vol. 100, p. 063120 (Feb. 2012), and "A method to fabricate disconnected silver nanostructures in 3D," published in Journal of Visualized Experiments, vol. 69, p. e4399 (2012), all of which are herein incorporated by reference in their entirety, can be employed to fabricate 3D patterns of a metallic structure in a polymeric matrix. By way of example, using these femtosecond direct-writing methods silver nanostructures with a minimum feature size of about 80 nm and a minimum spacing of about 150 nm can be generated in a polymeric matrix.

Some embodiments of zero index materials (ZIM) based on photonic Dirac-cone achieved by the modal degeneracy at the center of Brillouin zone may be lossy, e.g., because of the radiation loss at Γ point and/or material absorptions. Further, the existence of a Dirac-cone at Γ point can be sensitive to structural parameters. This can yield to low fabrication yield due to tolerances in the fabrication process. Various embodiments disclosed herein address this issue. For example, in one embodiment, an on-chip low-loss zero index material (LLZIM) with single mirror above a pillar array is disclosed. In another embodiment, an all-dielectric zero index material (AD-ZIM) with super-robust photonic Dirac-cone, which can be obtained by designing the pitch and height of a dielectric pillar array, is disclosed. As described further below, the concept of the robustness is demonstrated for frequencies in the telecommunications regime by measuring the refraction angles in photonic crystal prims fabricated according to the present teachings.

FIGs. 18A-18C schematically show exemplary embodiments of zero index photonic Dirac-cone (PDC) metamaterial structures according to the present teachings that and their representative *xy* mode distributions in single unit cell. Specifically, FIG. 18A shows a cross-sectional view of the structure shown and described above in relation to FIG. 6A, having pillars 1800 in SU-8 polymer, upper mirror 1802 (e.g. gold), lower mirror 1804, disposed on a SiO_2 layer 1806, which is in turn disposed on a silicon substrate 1808.

FIG. 18B shows a cross-sectional view of another embodiment of a ZIM structure with low loss, also referred to herein as low loss zero index metamaterial (LLZIM) having pillars 1800 in SU-8 polymer, a single upper mirror layer 1802, with the pillars being disposed on a SiO_2 layer 1806, which is in turn disposed on a Silicon substrate 1808.

FIG. 18C shows an embodiment of an AD-ZIM structure having dielectric pillars 1810 formed on a SiO_2 layer 1806, which is in turn disposed on a silicon substrate 1808.

Various structural parameters of the above embodiments can be adjusted so as to optimize those structures, e.g., to reduce loss, increase mode confinement, etc. As shown in FIG. 18A, some examples of such parameters include, without limitation, the lattice constant a, pillar radius r (or diameter $2r$), pillar height h_{Si}, the gold mirror thickness h_{Au}, and the thickness of SU-8 polymer $h_{SU\text{-}8}$ in the case of the ZIM shown in FIG. 18A, where $h_{SU\text{-}8}$ corresponds to the distance between top and bottom mirrors 1802 and 1804. In the embodiment of FIG. 18B, $h_{SU\text{-}8}$ corresponds to the distance between the top mirror and the surface of SiO_2. The structure of LLZIM in FIG. 18B may be the same as the structure of the ZIM shown in FIG. 18A, without bottom mirrors. In the case of the ADZIM shown in FIG. 18C, all the mirrors and SU-8 polymer layer are removed, and in some embodiments, the pillar height h_{Si} may be ~60% taller than the pillar heights in the other ZIMs.

FIGs. 18D, 18E, and 18F show the xy electromagnetic mode distributions calculated in single unit cell with periodic boundary conditions for the ZIMs in FIGs. 18A, 18B, and 18C. These are the original modes giving the electric and magnetic flux loops around the pillar. The shading shows Ez, and the black arrows show the H vector. Specifically, FIG. 18D shows a magnetic loop mode named as "Monopole mode," FIG. 18E shows an electric loop mode named as "Dipole mode," and FIG. 18F shows another degenerate "Dipole mode" forming the flat band but cannot be excited in this measurement. Here, the results are shown with the input k vector (k_x, k_y) of $(0, \pi/80a)$. Throughout this disclosure, the modes of FIGs. 18D and 18E are referred to as "Monopole mode" and "Dipole mode", respectively. The ZIM based on PDC is formed when the pillar geometry is optimized so that both modes are degenerated at Γ point. In some embodiments, there may also be another degenerated "Dipole mode" with an orthogonal

field distribution relative to that of the original Dipole mode as shown in FIG. 18F. This mode is always degenerate with the original Dipole mode at Γ point since their field distributions are essentially the same. In this case, this mode cannot be generated by applying a plane wave excitation since it has an odd distribution against the propagation direction *y*.

Periodic structures with single mirror, as shown in FIG. 18B, can confine the scattered light by tuning the spacing between the mirror and the periodic structure. In this case, a confinement against out-of-plane direction can guide resonance modes in the photonic crystal (PhC). To verify this theory for LLZIM, a single unit cell was simulated with a Si pillar with h_{Si} = 512 nm and perfect electric conductor (PEC) boundary at the top of the SU-8 layer as shown in FIG. 19A. FIG. 19B shows simulated quality factor (Q) and wavelength (λ) as a function of h_{SU-8} for the model in FIG. 19A. FIG. 19C is a schematic model of a unit cell with a realistic gold mirror having h_{Au} = 100 nm. FIG. 19D shows simulated Q and λ as a function of h_{SU-8} for the model in FIG. 19C.

By applying this model with *xy* periodic boundary condition, Q factor and λ of both modes as a function of h_{SU-8} for the model in FIG. 19A were calculated as shown in FIG. 19B. Here, structural parameters of a = 800 nm and r = 200 nm were used. These parameters are different from the optimized parameters described further below. In terms of the meaning of Q factor in this simulation, this Q is limited by the absorption loss of the material and that of perfect matching layer (PML) boundary (Q_{abs}), and the radiation loss that results from Γ point operation (Q_v) – therefore, Q can be expressed as $Q^{-1} = Q_{abs}^{-1} + Q_v^{-1}$.

The above simulations show that the monopole mode exhibits a substantially constant Q and λ as a function of h_{SU-8} except for the region $h_{SU-8} < 0.9$ μm. Without being limited to any particular theory, this is because the Monopole mode is one of the guided resonance modes in this type of pillar arrays, and hence it is not sensitive to the spacing or presence of the PEC boundary. In general, Q factor of guided resonance modes should be infinite, but in the unit cell, the evanescent tail of the mode is slightly absorbed by the bottom PML layer (thickness of SiO_2 layer is 2 μm, which is not large enough to neglect absorption by this layer), which results in a finite Q of around 10^5. Herein, this high Q is indicative of a loss-less behavior of the guided

resonance mode. On the other hand, for the Dipole mode, the clear phase interference effect is seen based on Fabry-Perot resonance between the mirror and the pillars. Such a Fabry-Perot resonance can result in a Q as high as that exhibited by the Monopole mode when h_{SU-8} is properly selected. λ is also changing accordingly, and this λ change tunes the degree of the phase interference. Therefore, high Q can be realized by placing the single mirror at the appropriate position. For the next step, the PEC boundary was changed based on a realistic gold mirror with h_{Au} =100 nm, and 2 μm-thick air layer with the PML layer outside of the gold mirror as shown in FIG. 19C. The Q factor and λ of both modes as a function of h_{SU-8} were calculated as shown in FIG. 19D. Because of the absorption loss of the gold, both Q factors are degraded. In the case of the Monopole mode, the absorption becomes almost comparable with the absorption of the PML layer when $h_{SU-8} \sim 1.5$ μm. On the other hand, the Dipole mode shows similar fringes appearing in FIG. 19B, but the Q factor is limited to ~ 1600 because of the gold absorption. In some embodiments, the Q factor for a LLZIM may be improved more than 30 times compared to a ZIM according to aspects disclosed herein. But still the Dipole mode's wavelength λ_{di} giving high Q does not match with the Monopole mode's wavelength λ_{mono} in this simulation; accordingly, there is a need for them to be the same for optimized LLZIM.

FIGs. 20A-20C show schematics illustrating optimization of one embodiment of an LLZIM by matching λ_{di} and λ_{mono} while maintaining a high Q. Since the Q of the Dipole mode is sensitive to λ_{di}, the Dirac-point with this λ_{di} must be found. This may be achieved conveniently by only changing λ_{mono} without changing λ_{di}. This operation is doable by changing two kinds of structural parameters properly. For example, λ_{di} may be changed with the structural change for *a* and *r*. FIG. 20A illustrates changing both *a* and *r* simultaneously so as to change only λ_{mono} while keeping λ_{di} constant. FIG. 20B shows λ_{di} and λ_{mono} as a function of the radio of *r* and *a* (*r/a*), indicating that λ_{di} remains substantially constant as λ_{mono} changes. The intersection of the two curves corresponds to the *r/a* that would lead to a Dirac-cone at Γ point . FIG. 20C shows Q for the monopole mode and the dipole mode are substantially insensitive to parameter *r/a*, e.g., for values of *r* and *a* shown in FIG. 21C.

FIGs. 21A and 21B show λ_{di} change with the structural change for *a* and *r* for an

embodiment where h_{Si} = 512 nm, $h_{SU\text{-}8}$ = 920 nm, h_{Au} =100 nm. Specifically, FIG. 21A shows λ_{di} as a function of a. FIG. 21B shows λ_{di} as a function of r. Both Figures show almost linear behavior, which can be approximated by linear functions. By fitting these curves with linear functions, slopes of $\Delta\lambda_{di}/\Delta a \sim 0.52$ nm/nm and $\Delta\lambda_{di}/\Delta r \sim 3.03$ nm/nm are obtained. According to the values of these slopes in FIG. 21A and 21B, a series of different pairs of a and r can be obtained as shown in FIG. 21C that keep λ_{di} constant. In other word, λ_{di} can be kept constant by tuning both a and r . On the other hand, usually λ_{mono} has different slopes compared to λ_{di}, so only λ_{mono} can shift by applying these parameters.

FIGs. 22A-22C illustrate utilizing the parameters depicted in FIG. 21C to render the monopole mode and the dipole mode degenerate at Γ point while maintain a high Q. FIGs. 22A and 22B show the change of λ and Q for both modes when the parameters in FIG. 21C are applied. Therefore, the modes behave in the same way as shown and described above in relation with FIGs. 20A-20C– the Dipole mode's Q is constant since λ_{di} is constant and only λ_{mono} shifts with the parameters to find Dirac-point. Specifically, FIG. 22A shows λ as a function of r/a. The crossing point of both modes indicates obtaining a Dirac-point with high Q. FIG. 22B shows Q as a function of the normalized radius r/a. By this optimization, optimal parameters of a = 815 nm, r = 196 nm, $h_{SU\text{-}8}$ = 920 nm, h_{Si} = 512nm and h_{Au} = 100 nm are obtained for an embodiment of LLZIM with a single gold mirror. FIG. 22C shows the simulated band structure around the Γ point with these optimal parameters. Additionally, FIG. 23 shows the simulated 3D dispersion surfaces of the Monopole mode and Dipole mode in the rage of (k_x, k_y) = ([-X/4 X/4], [-M/4 M/4]) for the embodiment having the same parameters as FIG. 22C. FIG. 23 clearly shows a PDC, and the dispersion around the Γ point exhibits a more linear-like behavior compared to an embodiment of the ZIM with double mirrors. Thus, an LLZIM with 30 times higher Q has been obtained theoretically through the above simulations and optimizations.

In other embodiments, another dielectric multiple layer mirror may be used instead of gold, to realize an LLZIM with a lower loss. In such embodiments, the loss may only be limited by the scattering loss, e.g., due to fabrication imperfections.

As shown and described above in relation with FIG. 18C, another embodiment disclosed herein is an AD-ZIM. One advantage of AD-ZIMs is that in many embodiments they are robust against structural variations, for example due to fabrication errors, thus making them easier to fabricate for practical use. Robustness may be achieved even with simple AD-ZIM structures.

FIGs. 24A-24C schematically demonstrate robustness of an AD-ZIM according to an embodiment in comparison to a ZIM with a double mirror. FIG. 24A shows mode wavelength λ as a function of r for a ZIM having a double mirror, as shown for example in FIG. 18A, and having parameters a = 690 nm, h_{Si} = 512 nm, $h_{SU\text{-}8}$ = 1.25 mm, and h_{Au} = 100 nm. As described above in relation with the LLZIM, both modes have different slopes $\Delta\lambda/\Delta r$, so the degeneracy never happens without having a proper value of r. In a typical fabrication process, the fabrication error associated with r is dominant more than those associated with a and h_{Si}, so this characteristic may degrade the robustness of a ZIM with double mirrors. On the other hand, FIG. 24B shows an AD-ZIM (*See* also FIG. 18C) with pillars ~ 59% taller than the pillars of the ZIM shown in FIG. 24A, with h_{Si} = 815 nm, and a = 879 nm. FIG. 24B further shows λ as a function of r for the AD-ZIM. Once the structural parameters are selected properly in ADZIM, both modes exhibit almost the same slope and the same λ for the same pillar radius, as shown in FIG. 24B. This behavior makes forming PDC more robust and stable. In some embodiments, the PDC need not be perfect, but may be near or substantially a PDC, having a narrow bandgap that is substantially zero. Near PDCs whose bandgap is substantially small exhibit useful behavior.

FIG. 24C shows the calculated band diagrams around the Γ point with five different sizes of $2r$ ($2r$ = 474 nm, 484 nm, 493 nm, 503 nm and 512 nm respectively) for the AD-ZIM of FIG. 24B. All of these implementations show near PDC behavior with a certain range of r. An aspect of robustness is that the λ of zero index may be tuned by changing r and keeping a constant. Thus, in some embodiments, further optimizations may not be necessary to connect AD-ZIMs with different λ of zero index in various applications.

FIG. 25 shows calculated 3D dispersion surfaces of a robust AD-ZIM with a = 918 nm, h_{Si} = 850 nm, r = 250 nm, and k vector (k_x, k_y) of ([-M/4 M/4], [-X/4 X/4]). In the case of some AD-ZIMs, the dispersion around the Γ point becomes more quadratic shaped in comparison to

other ZIMs. Thus, in some embodiments, near zero index may be achieved even if k is slightly shifted from Γ.

In some embodiments, an effective refractive index of a unit cell of metamaterial according to the present teachings can be used to determine values for structural parameters of the metamaterial, e.g., the radius, and periodicity of the pillars. For example, a mode equivalent index n_{eq} can be calculated using the following relationship of $n_{eq}{}^2 = \sum_{m=1}^{n} \eta_m n_m{}^2$, where n is the index of each material part in a unit cell. Basically, the index sensitivity of the resonant mode is proportional to $n_{eq}{}^{-1}$. Thus, $\Delta\lambda/\Delta r$ could also have a similar relationship with $n_{eq}{}^{-1}$ if the perturbation of r is substantially small.

FIGs. 26A-26B show verification of the relationship between n_{eq} and $\Delta\lambda/\Delta r$. To verify this relationship, n_{eq} is calculated for both modes with different pillar heights h_{Si} as shown in FIG. 26A, for an AD-ZIM embodiment having a = 879 nm and r = 256 nm, and where the material index of Si, n_{Si} = 3.42, and of SiO_2, n_{SiO2} = 1.45. The graph in FIG. 26A shows that the n_{eq} of both modes are equal when h_{Si} = 885 nm. FIG. 26B shows modal wavelength λ as a function of r for an embodiment where a = 879 nm and h_{Si} = 885 nm, which corresponds to the n_{eq} of both modes being equal, resulting in equal or substantially equal slopes for both modes. According to this simulation result, two constrains must be satisfied in some embodiments to design a robust ADZIM; 1) $\lambda_{mono} = \lambda_{di}$, and 2) $n_{eq\_mono} = n_{eq\_di}$. To satisfy these two conditions, $\Delta\lambda/\Delta a$, $\Delta\lambda/\Delta h_{Si}$ and $\Delta n_{eq}/\Delta a$, $\Delta n_{eq}/\Delta h_{Si}$ were investigated for both modes in order to design proper a and h_{Si}.

FIGs. 27A-27D show investigation of the dependences of modal wavelength and modal equivalent index on structural parameters to design a robust AD-ZIM. Specifically, FIG. 27A shows λ as a function of h_{Si}. FIG. 27B shows λ as a function of a. FIG. 27C shows n_{eq} as a function of h_{si}, and FIG. 27D shows n_{eq} as a function of a. In one embodiment, linear approximations may be applied for all the curves. Thus, λ_{mono}, λ_{di}, n_{eq_mono} and n_{eq_di} may be expressed by using the coefficients of A, B, C, D, E, F, A', B', C', D', E', F':

$$\lambda_{mono} = Ah_{Si} + Ba + C,$$

$$\lambda_{\mathrm{di}} = A' h_{\mathrm{Si}} + B' a + C',$$

$$n_{\mathrm{eq\_mono}} = D h_{\mathrm{Si}} + E a + F,$$

$$n_{\mathrm{eq\_di}} = D' h_{\mathrm{Si}} + E' a + F'.$$

The coefficients may be derived from the approximated functions. By substituting the aforementioned two constrains $\lambda_{\mathrm{mono}} = \lambda_{\mathrm{di}}$ and $n_{\mathrm{eq\_mono}} = n_{\mathrm{eq\_di}}$ into these equations, a solution of a = 967 nm and h_{Si} = 897 nm may be obtained. By applying these solved parameters, the optimized robustness was confirmed within the range of r = 0.24 – 0.30 as shown in FIG. 28A, which shows λ as a function of r with the solved parameters (a = 967 nm, h_{Si} = 897 nm, the inset also shows the same parameters). FIG. 28A shows that the modal wavelengths became equal at wavelengths larger than telecommunications wavelength. In various embodiments, λ may be affected by scaling up or down the radius of the pillars. FIGs. 28A to 28D show λ as a function of r with the scaling factor of 88%, 90%, 92%, and 94% respectively. This shows that λ can be tuned to a wavelength within the telecommunications regime by scaling the size of the pillars. Therefore, robustness is maintained with different λ, which means the robustness in an AD-ZIM follows the scaling law. Conveniently, this robustness is referred to herein as "super-robustness."

FIGs. 29A-29C show optical microscope images of one embodiment of a fabricated on-chip super-robust AD-ZIM prism device as described above. Further, FIG. 30A shows SEM images of the same fabricated device with the optimized parameters shown and described in relation with FIGs. 29A-29C. Specifically, FIG. 29A shows a photonic chip showing waveguides 2900 and 2902, and AD-ZIM prisms 2904. FIG. 29B shows a zoomed image FIG. 29A, showing the fabricated prism 2904 with silicon waveguide 2902 and SU-8 slab waveguide 2900. FIG. 29C shows a zoomed image of FIG. 29B, showing the prism 2904, which is a right triangular array of all dielectric pillars. More than 20 prism devices with different r were fabricated on the same chip, and each of them was connected to a Si tapered waveguide exciting a plane wave for the input and a semicircular SU-8 slab waveguide to observe the refracted beam output from the prism. To make the scattered light at the edge of the SU-8 slab waveguide more visible, semicircular gold bottom mirrors 2906 were also deposited at the bottom along the SU-8 slab waveguide, as shown in FIG. 29B. Another SU-8 waveguide 2908 surrounding the SU-8 slab

waveguide 2900 was used, as shown in FIG. 29B, to observe the scattering light from the gold markers (the relative positions along the SU-8 slab waveguide at -90°, -45°, 45°, and 90°) which indicate the accurate position of the prism for image processing and finding the refracted angle φ as shown in FIG. 30A.

AD-ZIM devices may be fabricated, for example, by a method similar to the method described above in relation to FIG. 7. In one embodiment, AD-ZIM prisms and devices may be fabricated through clean room processes consisting of e-beam lithography and ICP-RIE dry etching, in a manner similar to the methods of fabrication for a ZIM with double mirrors discussed above. But the fabrication steps may be simpler compared to those used for fabricating a ZIM with double mirrors. In one embodiment, a silicon-on-insulator (SOI) wafer may be used with a Si layer of ~850 nm, which is obtained by Si regrown on SOI (e.g., the original thickness of Si layer can be 512 nm). The robustness for this new thickness may be reoptimized, and by using a = 918 nm, the robustness satisfying the criteria of near PDC can be obtained in the range of r = 240 nm – 275 nm with the operation λ being around 1600 nm. FIGs. 29A-29C show optical microscope images and FIG. 30A shows SEM images of the fabricated device with the optimized parameters.

FIG. 30B shows one example of the near field pattern of the scattered light along the edge of the SU-8 slab waveguide 2900, where the white dotted line denotes the edge of the SU-8 slab waveguide 2900. The image was obtained using a near infrared camera, showing scattered light around the prism device with $2r$ = 459 nm when 1570 nm laser light was input from the Si tapered waveguide 2902. Since the prism is not covered by any metal mirrors, the scattering light at the prism is stronger, and the scattered light coming from the refracted beam of the prism is clearly observed at the edge of the SU-8 slab waveguide.

FIG. 30C shows the angular intensity distribution along the edge of the SU-8 slab waveguide 2900 with different λ input from 1480 nm – 1680 nm, and for different devices having $2r$ = 459 nm, 485 nm and 503 nm respectively. These distributions show that the refraction angle φ changes linearly and gradually around 1500 nm – 1650 nm, and it also crosses at zero degree with ~1560 nm, indicating that AD-ZIM is obtained at that λ. Moreover, other

prisms with different *2r* have also been measured, and show similar behavior with different λ regimes. To quantify φ for each prism with different λ input, 2D Gaussian fitting may be applied to the near field patterns to obtain the estimated n_{eff} with error bars, as shown in FIG. 30D. Based on these results, the zero index λ becomes longer when *2r* becomes larger, which is consistent with the simulation results as shown and described above in relation with FIG. 7C. These results show that super-robustness of the designed AD-ZIM is achieved.

Accordingly, various embodiments disclosed herein include ZIMs with double mirrors, LLZIMs and super-robust AD-ZIMs with more simplified structures than ZIMs with double mirrors. Various embodiments of LLZIMs have structures which provide zero index with 30 times better loss by phase destructive interference of the Dipole mode with a proper mirror spacing. Various embodiments of AD-ZIMs and methods of designing super-robust AD-ZIMs are also disclosed. Super-robust AD-ZIMs have been fabricated, and measured on-chip prism devices have demonstrated zero index operation. Robustness allows an on-chip ZIM platform for any operational λ which can be useful for achieving practical applications.

Those having ordinary skill in the art will appreciate that various changes can be made to the above embodiments without departing from the scope of the invention.

All of the publications disclosed herein are incorporated by reference in their entirety.

Claims:

1. A photonic structure, comprising:

a plurality of periodically repeating structures, said structures being configured and arranged relative to one another such to form a photonic crystal exiting any of a Dirac cone or near Dirac-cone at the center of the Brillouin zone of its reciprocal lattice for at least one wavelength in the optical regime.

2. The photonic structure of claim 1, wherein said Dirac cone is at a wavelength in a range of about 400 nm to about 100 μm.

3. The photonic structure of claim 1, wherein said repeating structures comprise a plurality of pillars.

4. The photonic structure of claim 3, wherein said pillars have substantially cylindrical shapes with a radius of about 1/8 of said at least one wavelength.

5. The photonic structure of claim 4, wherein said pillars have a maximum height of about 1/3 of said at least one wavelength.

6. The photonic structure of claim 3, wherein said pillars have a height in a range of about 30% to about 60% of the wavelength at the Dirac-cone or the near Dirac-cone.

7. The photonic structure of claim 5, wherein said pillars exhibit a periodicity in each of two orthogonal dimensions in a plane perpendicular to their heights characterized by a lattice constant (a) such that a ratio of radius of said pillars to said lattice constant (r/a) is in a range of about 0.2 to about 0.3.

8. The photonic structure of claim 3, wherein said pillars comprise a dielectric material exhibiting a real refractive index contrast relative to a material surrounding the pillars that is greater than about 1.

9. The photonic structure of claim 3, wherein said pillars comprise any of silicon, diamond, TiO2, silicon nitride (Si_3N_4), aluminum oxide, InGaAsP, GaN, and InGaN.

10. The photonic structure of claim 3, wherein said pillars are disposed on a surface of a dielectric substrate.

11. The photonic structure of claim 10, wherein said dielectric substrate exhibits a real refractive index less than a real refractive index of a material of said pillars.

12. The photonic structure of claim 3, wherein said dielectric substrate comprises any of SiO_2, sapphire, InP, PDMS, Cytop, SU-8 and PMMA.

13. The photonic structure of claim 10, further comprising a top metallic layer disposed on top surfaces of said pillars.

14. The photonic structure of claim 13, further comprising a bottom metallic layer disposed on at least a portion of said surface of the dielectric substrate on which the pillar are disposed.

15. The photonic structure of claim 14, wherein each of said top and bottom metallic layers has a thickness in a range of about 50 nm to about 100 nm.

16. The photonic structure of claim 15, wherein each of said metallic layers comprises any of gold and silver.

17. The photonic structure of claim 3, wherein said pillars are sandwiched between two metallic layers.

18. The photonic structure of claim 17, wherein each of said metallic layers has a thickness in a range of about 50 nm to about 100 nm.

19. The photonic structure of claim 3, wherein said photonic structure exhibits a substantially vanishing real refractive index at said at least one wavelength.

20. The photonic structure of claim 19, wherein said photonic structure exhibits a non-zero real impedance at said at least one wavelength.

21. The photonic structure of claim 20, wherein said non-zero impedance is tunable by adjusting pitch and radius of said pillars.

22. The photonic structure of claim 1, wherein said photonic structure exhibits a Q factor greater than about 20 for at least two substantially degenerate states having a vanishing wavevector.

23. The photonic structure of claim 3, wherein said photonic crystal exhibits an imaginary refractive index less than about 0.1 at said at least one wavelength.

24. The photonic structure of claim 10, wherein said pillars are disposed in a resin.

25. The photonic structure of claim 23, wherein said resin comprises any of SU8, Cytop, PMMA, and PDMS.

26. The photonic structure of claim 24, wherein said resin has a height in a range of about 50 nm to about 100 nm.

26. A photonic crystal, comprising:

a plurality of periodically repeating structures, said structures being configured and arranged relative to one another such as to form a band structure providing at least two substantially degenerate states at the center of the Brillouin zone of a reciprocal lattice of the photonic crystal for at least one wavelength in the optical regime.

27. The photonic crystal of claim 26, wherein said repeating structures comprise a plurality of pillars.

28. The photonic crystal of claim 27, wherein said pillars comprise a dielectric material exhibiting a real refractive index contrast relative to a material surrounding the pillars that is greater than about 1.

29. The photonic crystal of claim 27, wherein said pillars have substantially cylindrical shapes with a radius of about 1/8 of said at least one wavelength.

30. The photonic crystal of claim 29, wherein said pillars have a maximum height of about 1/3 of said at least one wavelength.

31. The photonic crystal of claim 30, wherein said pillars exhibit a periodicity in each of two orthogonal dimensions in a plane perpendicular to their heights characterized by a lattice constant (a) such that a ratio of radius of said pillars to said lattice constant (r/a) is in a range of about 0.2 to about 0.3.

32. The photonic crystal of claim 27, wherein said pillars comprise any of silicon, diamond, TiO2, silicon nitride, aluminum oxide, InGaAsP, GaN, and InGaN.

33. The photonic crystal of claim 26, wherein said photonic crystal exhibits a Q factor greater than about 20 for said at least two substantially degenerate states having a vanishing wavevector.

34. An integrated photonic device, comprising:

a substrate,

a photonic crystal disposed on said substrate, said photonic crystal exhibiting a Dirac cone the center of the Brillouin zone of its reciprocal lattice for at least one wavelength in the optical regime,

an input port for receiving radiation and an output port optically coupled to said photonic crystal for transmitting at least a portion of said received radiation to said photonic crystal, and

an output waveguide disposed on said substrate, said output waveguide having an input port for receiving at least a portion of the radiation transmitted through the photonic crystal.

35. The integrated photonic device of claim 34, wherein said output port of the output waveguide is configured for optical coupling to a downstream component of the photonic device.

36. The integrated photonic device of claim 34, wherein said substrate comprises silicon.

37. The integrated photonic device of claim 34, further comprising a silicon dioxide layer disposed between a top surface of said substrate and said photonic crystal.

38. The integrated photonic device of claim 34, wherein said pillars comprise silicon.

39. The integrated photonic device of claim 34, further comprising a resin in which said pillars are disposed.

40. The integrated photonic device of claim 34, wherein said input waveguide is configured to transmit said radiation into the photonic crystal in plane of said pillars.

41. The integrated photonic device of claim 40, wherein said output waveguide is configured to receive the radiation transmitted through the photonic crystal in plane of said pillars.

42. A photonic structure, comprising:

a plurality of periodically repeating structures, said structures being configured and arranged relative to one another such as to form a photonic crystal,

wherein said photonic structure exhibits a substantially vanishing real refractive index and a non-zero impedance for at least one wavelength in the optical regime.

43. The photonic structure of claim 42, wherein said photonic structure exhibits a Q factor greater than about 20 at said at least one wavelength.

44. The photonic structure of claim 42, wherein said periodically repeating structures comprise a plurality of pillars.

45. The photonic structure of claim 44, wherein said pillars have substantially cylindrical shapes with a radius of about 1/8 of said at least one wavelength.

46. The photonic structure of claim 45, wherein said pillars have a maximum height of about 1/3 of said at least one wavelength.

47. The photonic structure of claim 46, wherein said pillars exhibit a periodicity in each of two orthogonal dimensions in a plane perpendicular to their heights characterized by a lattice constant (a) such that a ratio of radius of said pillars to said lattice constant (r/a) is in a range of about 0.2 to about 0.3.

48. The photonic structure of claim 44, wherein said pillars comprise any of silicon, diamond, TiO2, silicon nitride, aluminum oxide, InGaAsP, GaN, and InGaN.

49. The photonic structure of claim 42, wherein said photonic structure exhibits a Q factor greater than about 1500 at said at least one wavelength.

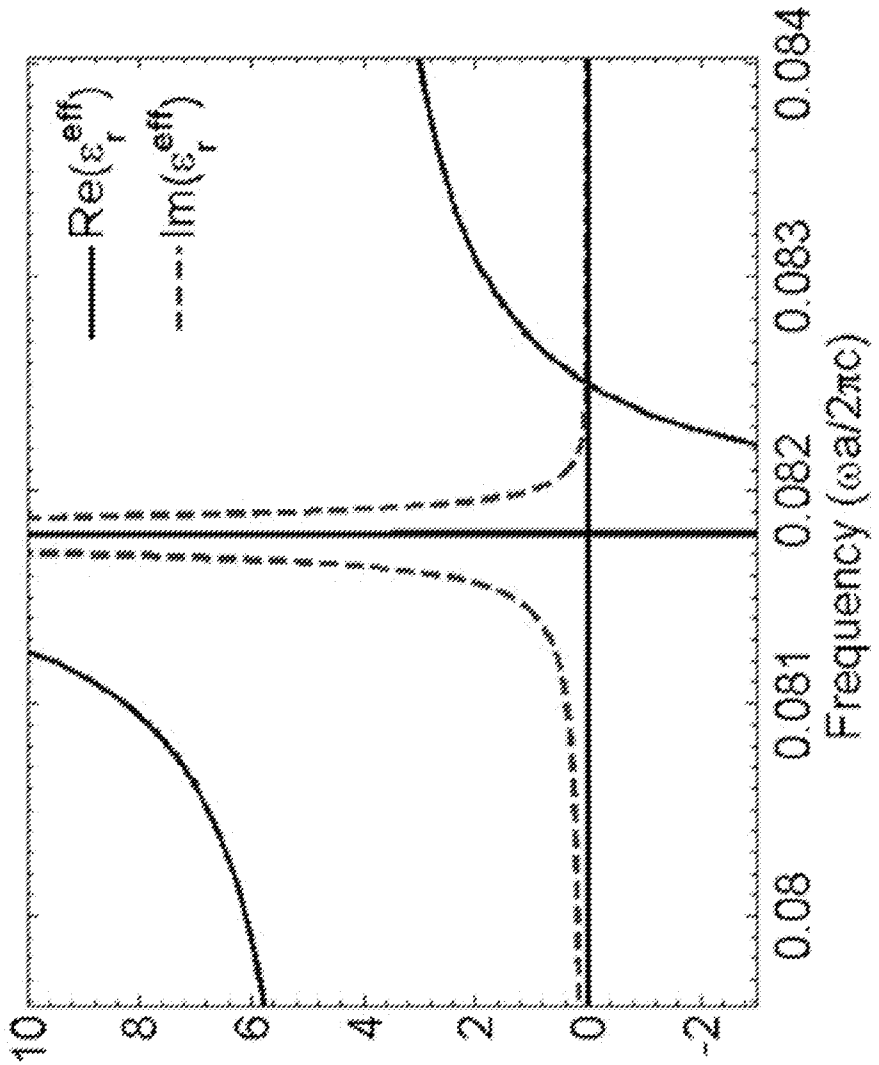
Re(ε_r^{eff})
Im(ε_r^{eff})
10
8
6
4
2
0
-2
0.08
0.081
0.082
0.083
0.084
Frequency (ωa/2πc)

FIG. 1

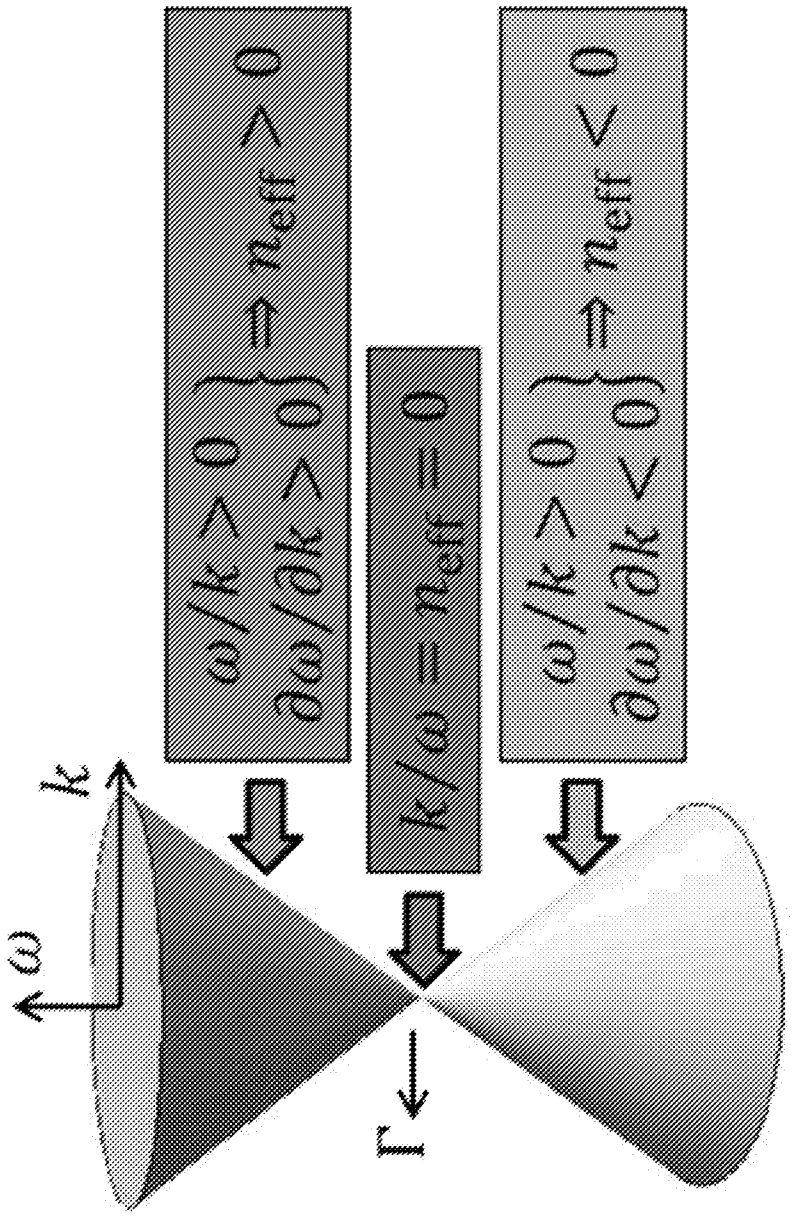

FIG. 2

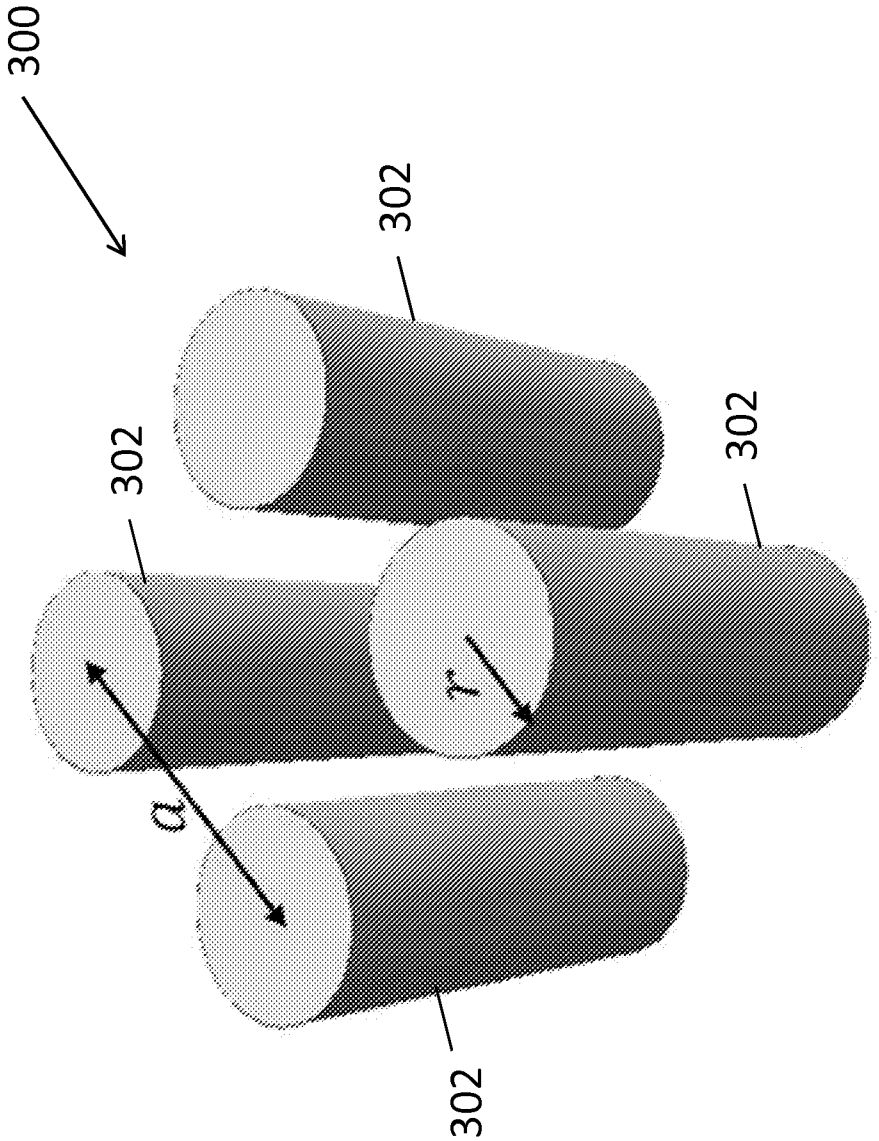

FIG. 3

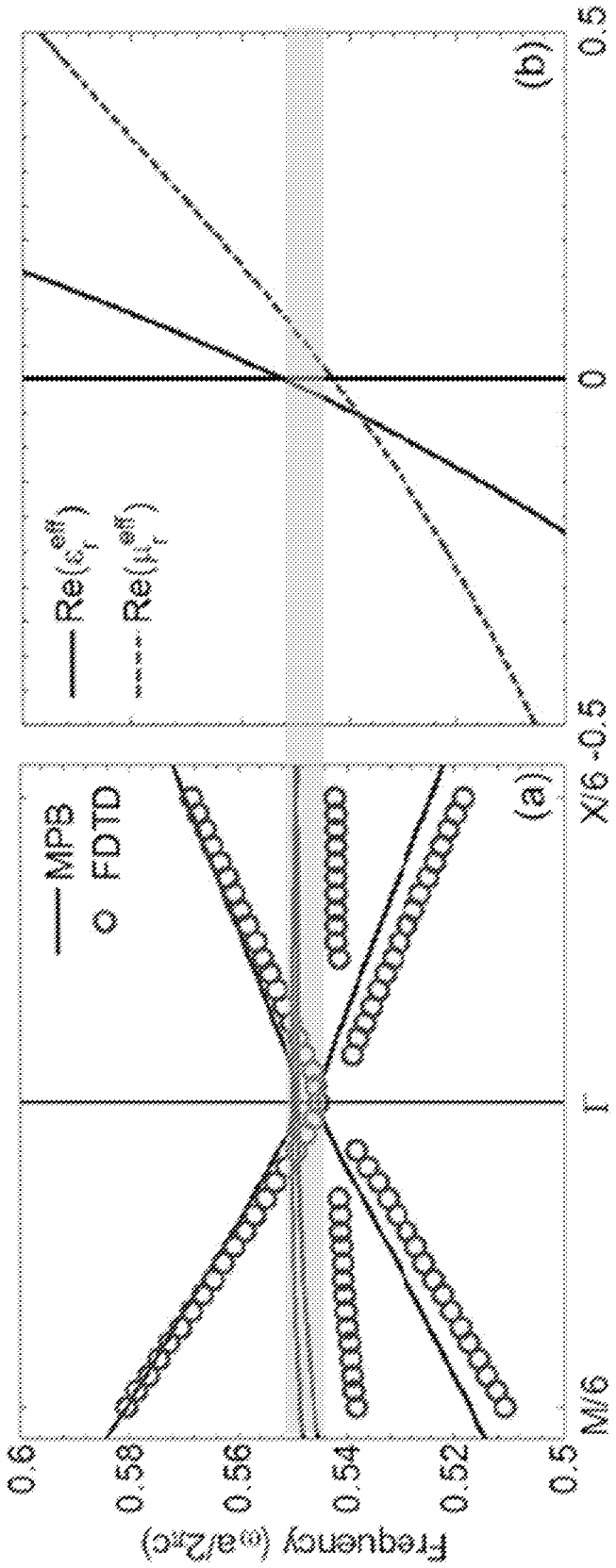
Frequency (ωa/2πc)
0.6
0.58
0.56
0.54
0.52
0.5
M/6
Γ
X/6
-0.5
0
0.5
(a)
(b)
MPB
FDTD
Re(ε_r^eff)
Re(μ_r^eff)

FIG. 4A

FIG. 4B

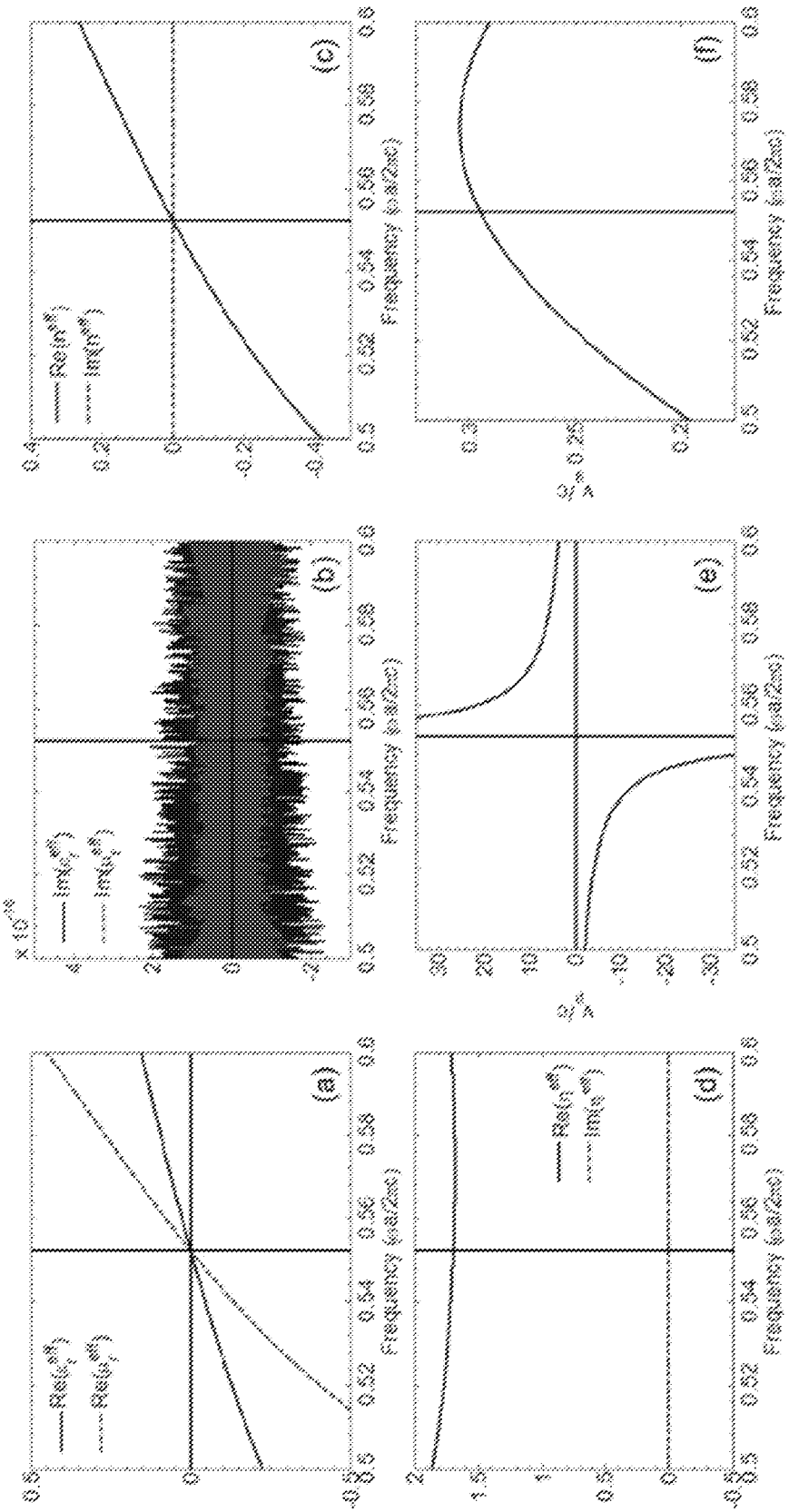

FIG. 5A FIG. 5B FIG. 5C

FIG. 5D FIG. 5E FIG. 5F

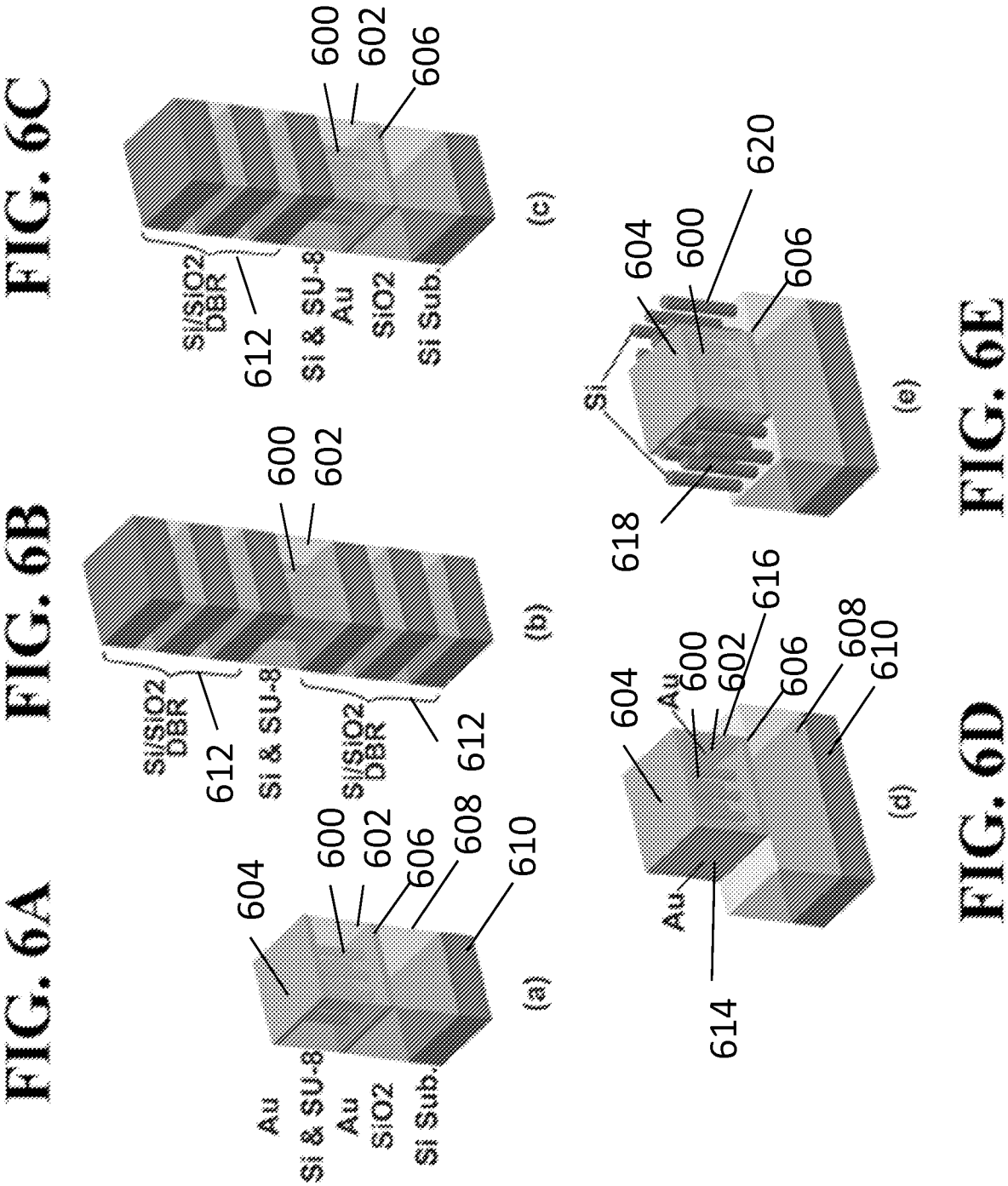

FIG. 6A FIG. 6B FIG. 6C FIG. 6D FIG. 6E

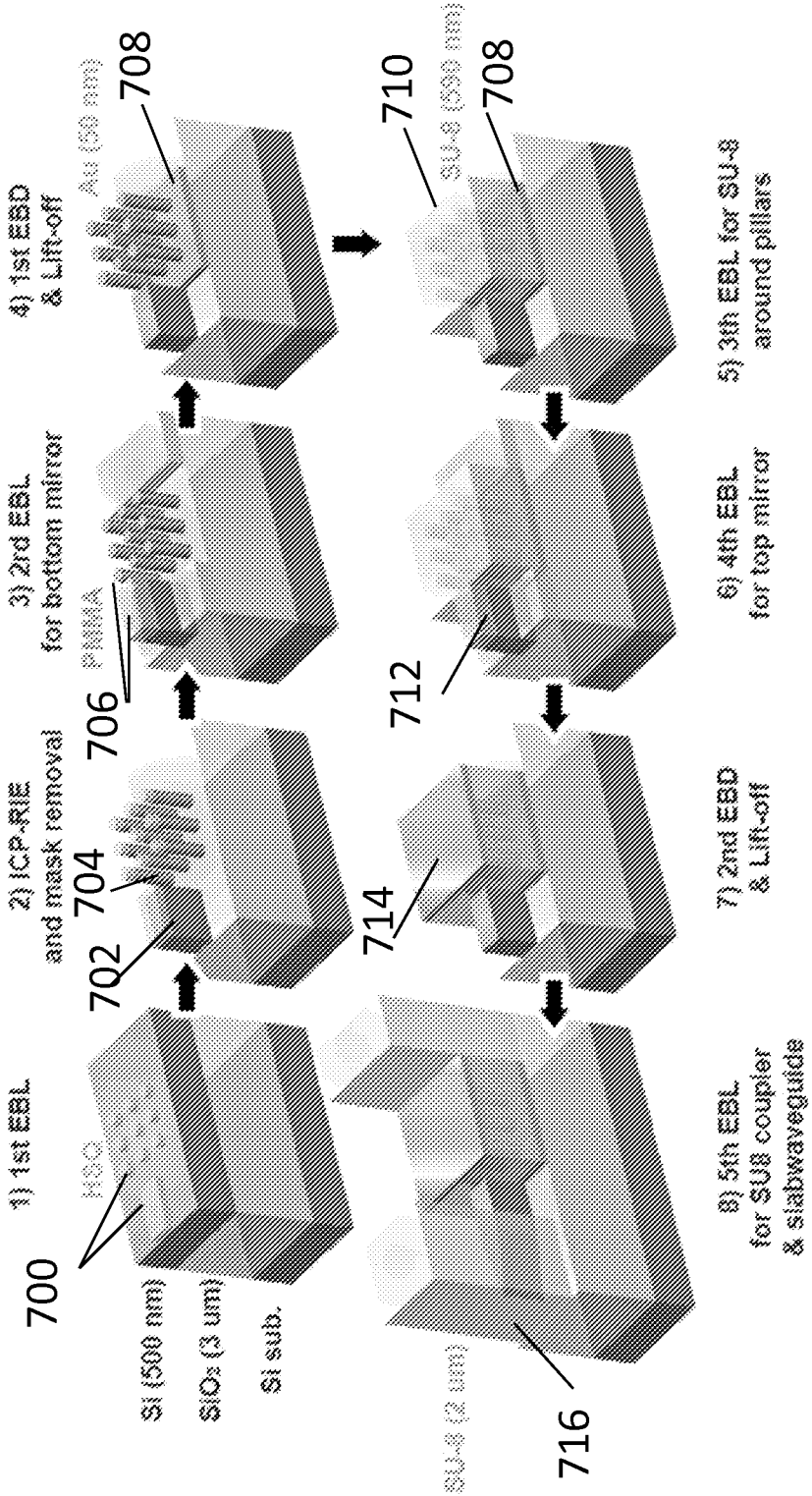
1) 1st EBL
HSQ
Si (500 nm)
SiO2 (3 um)
Si sub.
700
2) ICP-RIE
and mask removal
702
704
3) 2nd EBL
for bottom mirror
PMMA
706
4) 1st EBD
& Lift-off
Au (50 nm)
708
5) 3th EBL for SU-8
around pillars
SU-8 (500 nm)
710
6) 4th EBL
for top mirror
712
7) 2nd EBD
& Lift-off
714
8) 5th EBL
for SU8 coupler
& slabwaveguide
SU-8 (2 um)
716

FIG. 7

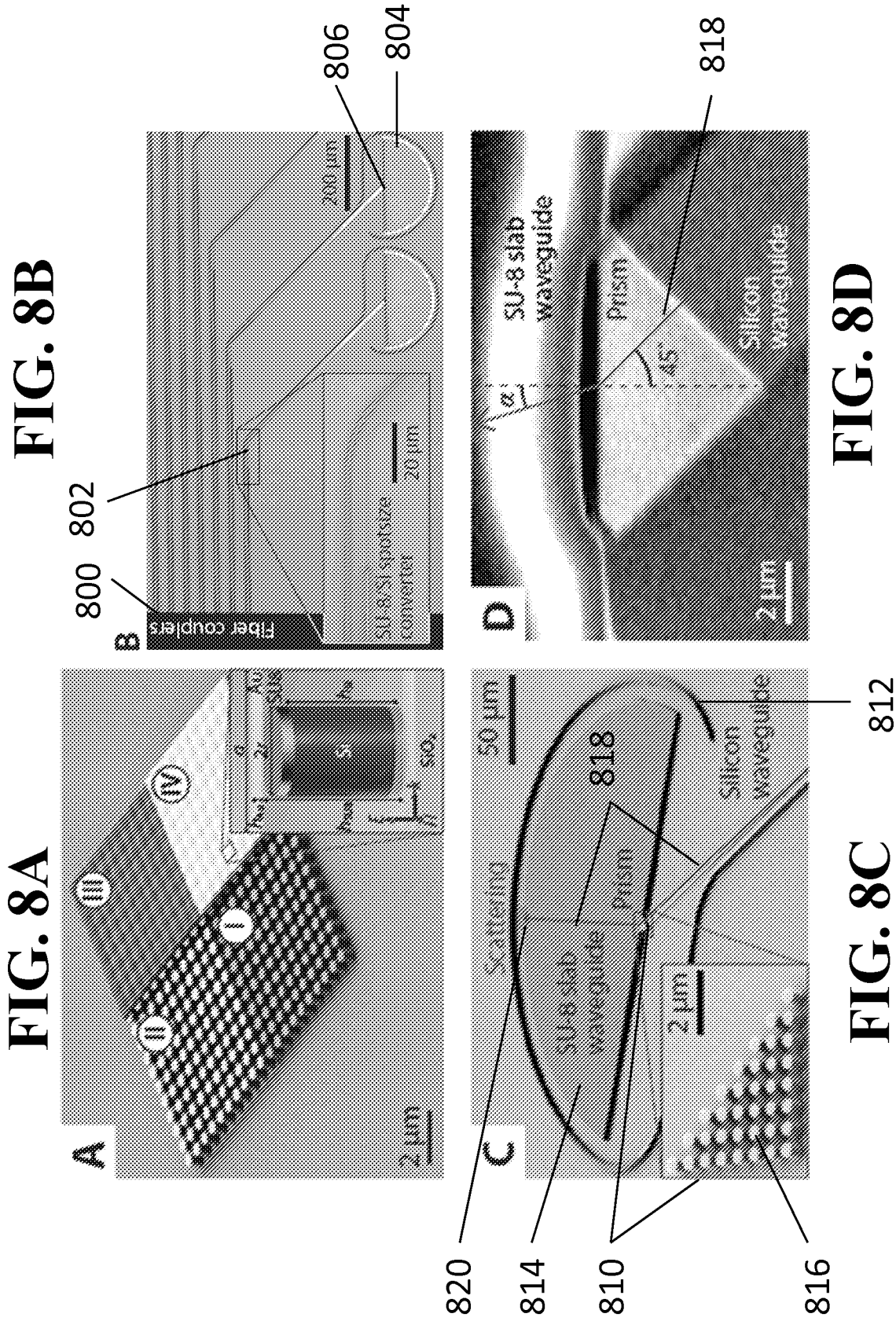

FIG. 8A

FIG. 8B

FIG. 8C

FIG. 8D

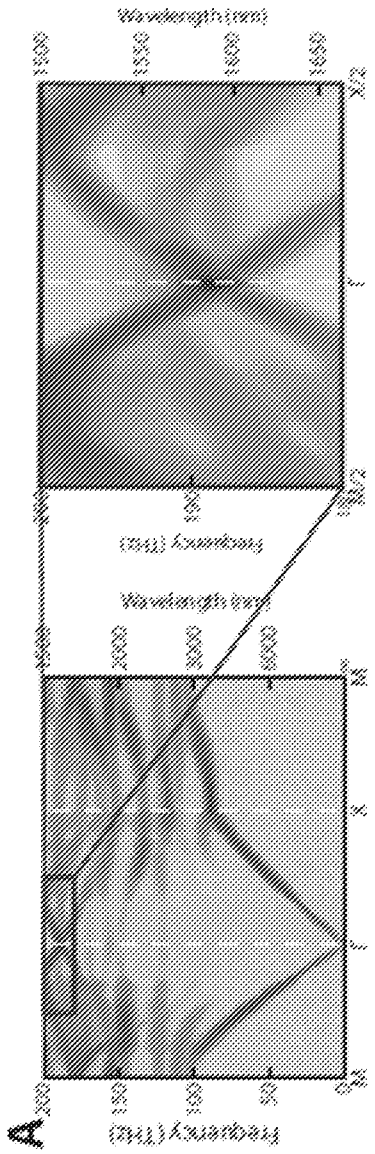

FIG. 9A

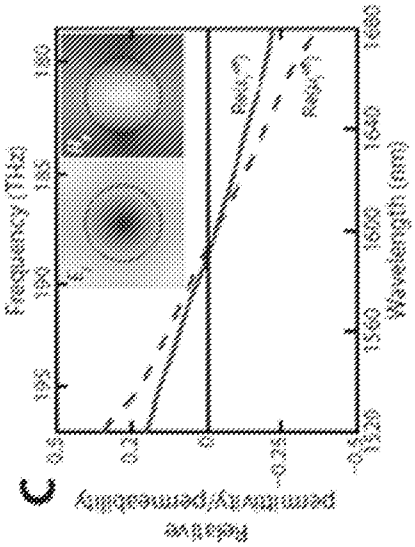

FIG. 9C

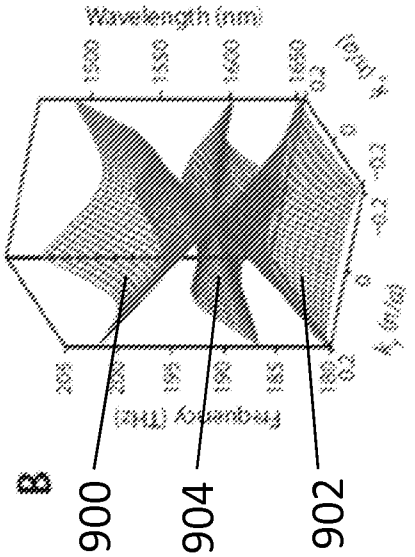

FIG. 9B

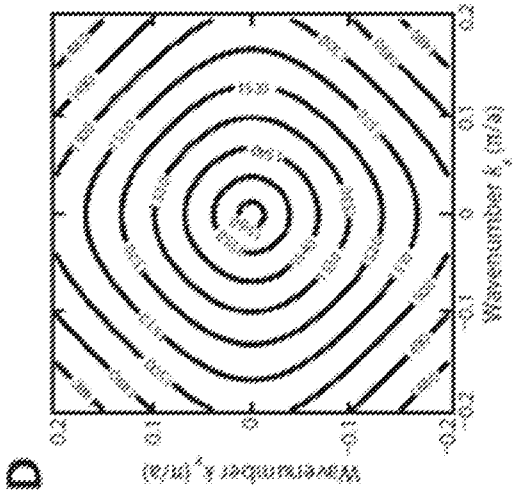

FIG. 9D

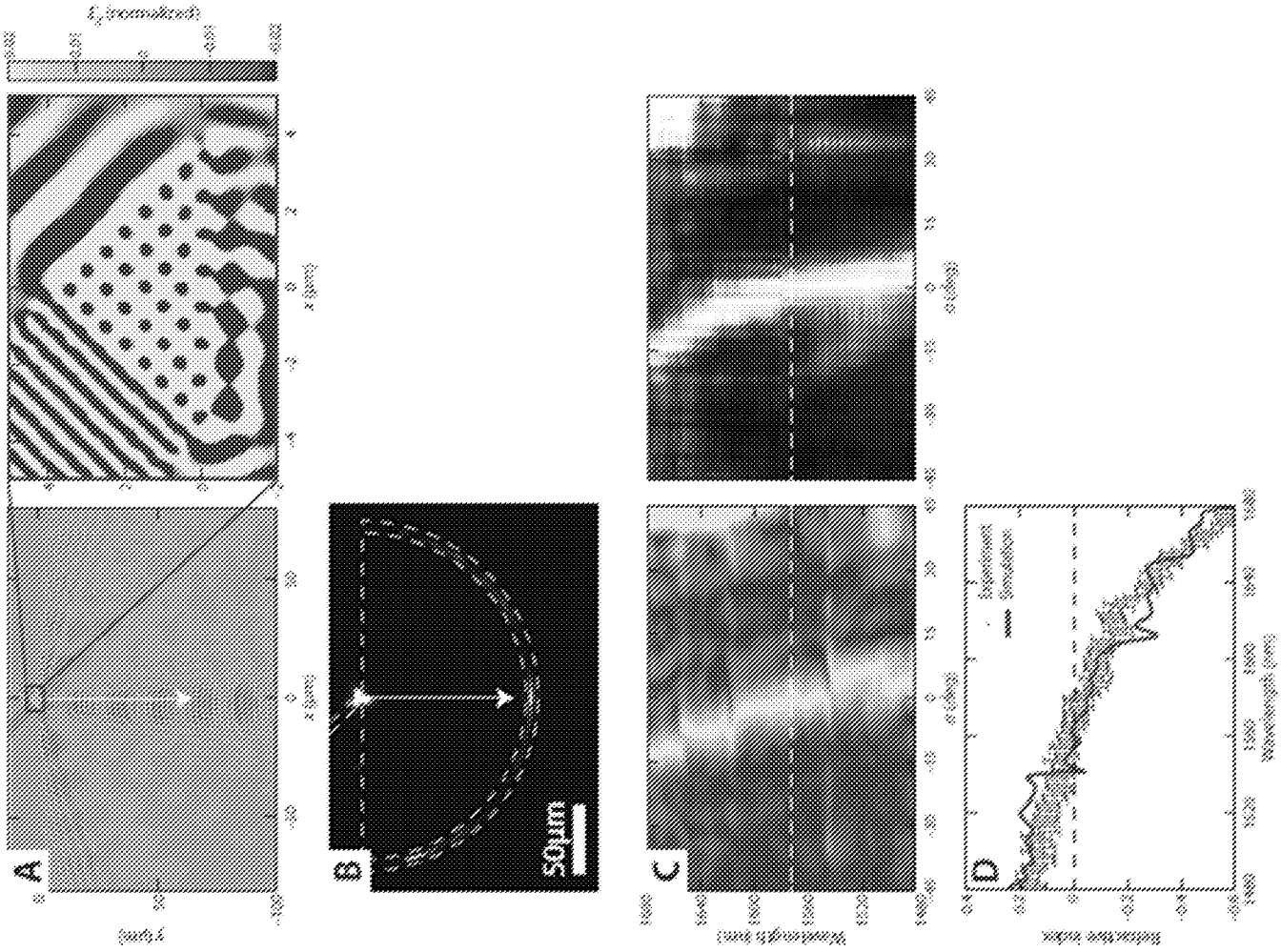

FIG. 10A

FIG. 10B

FIG. 10C

FIG. 10D

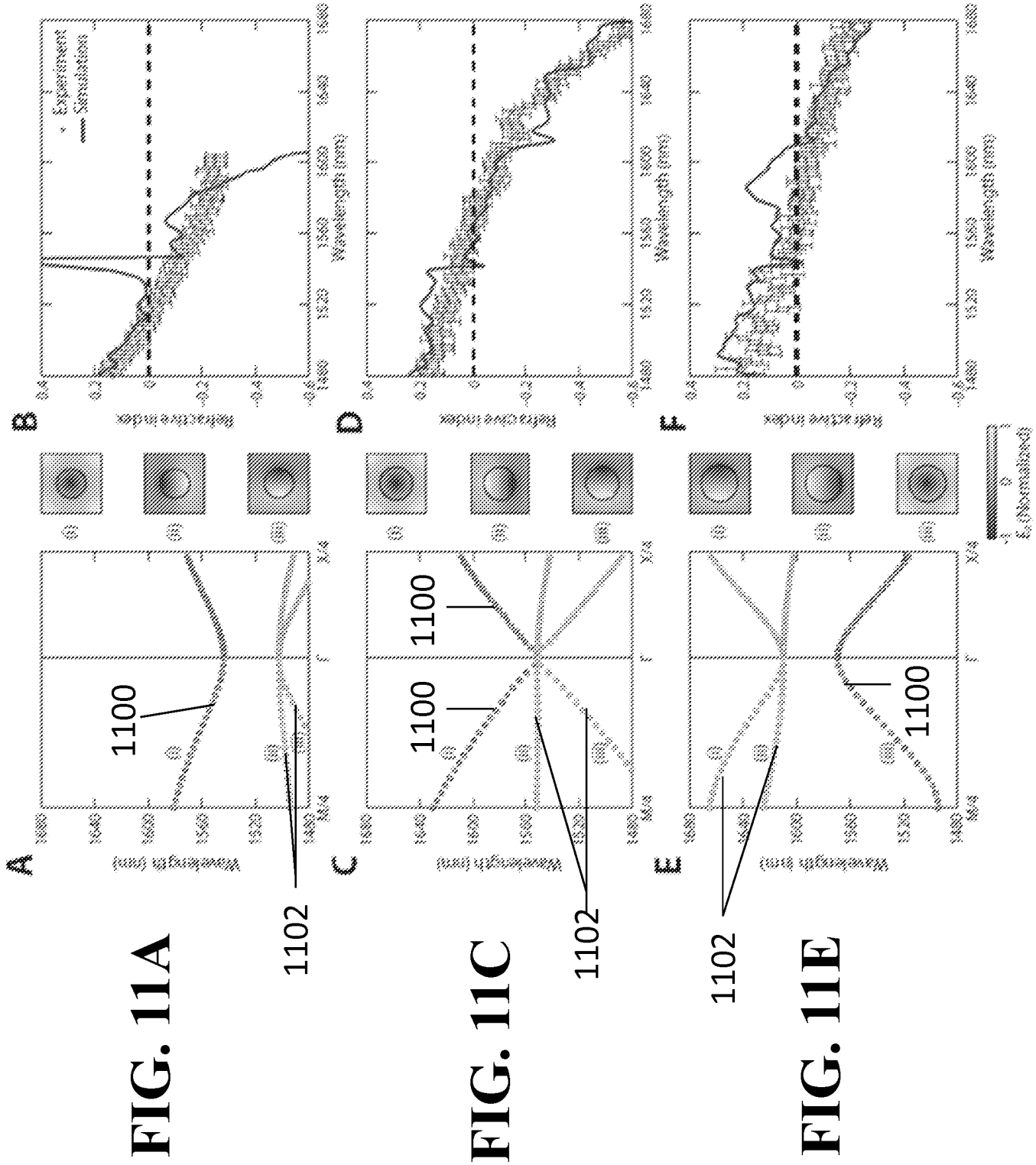

FIG. 11A

FIG. 11B

FIG. 11C

FIG. 11D

FIG. 11E

FIG. 11F

FIG. 12A

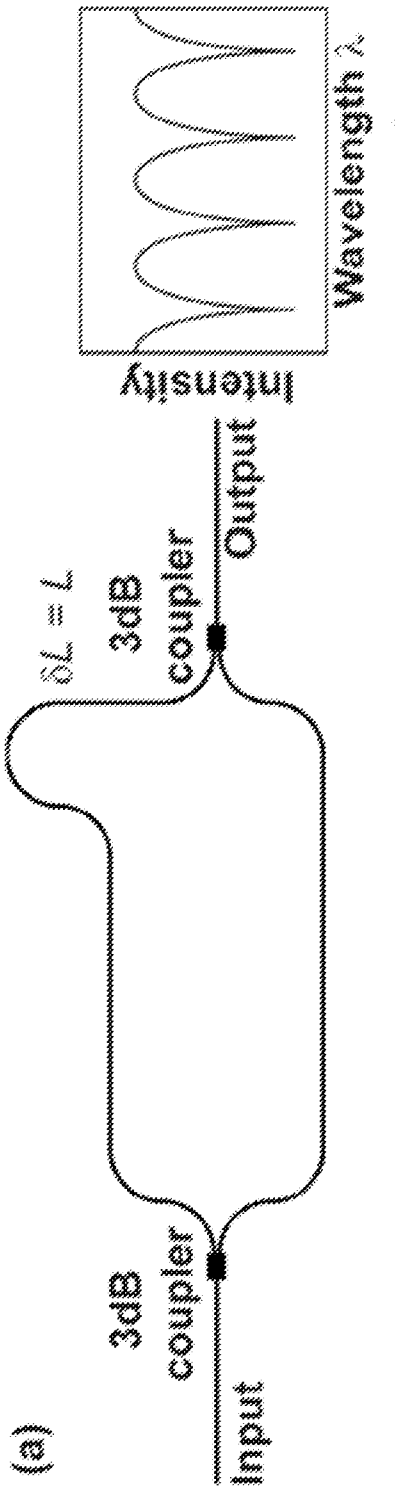

FIG. 12B

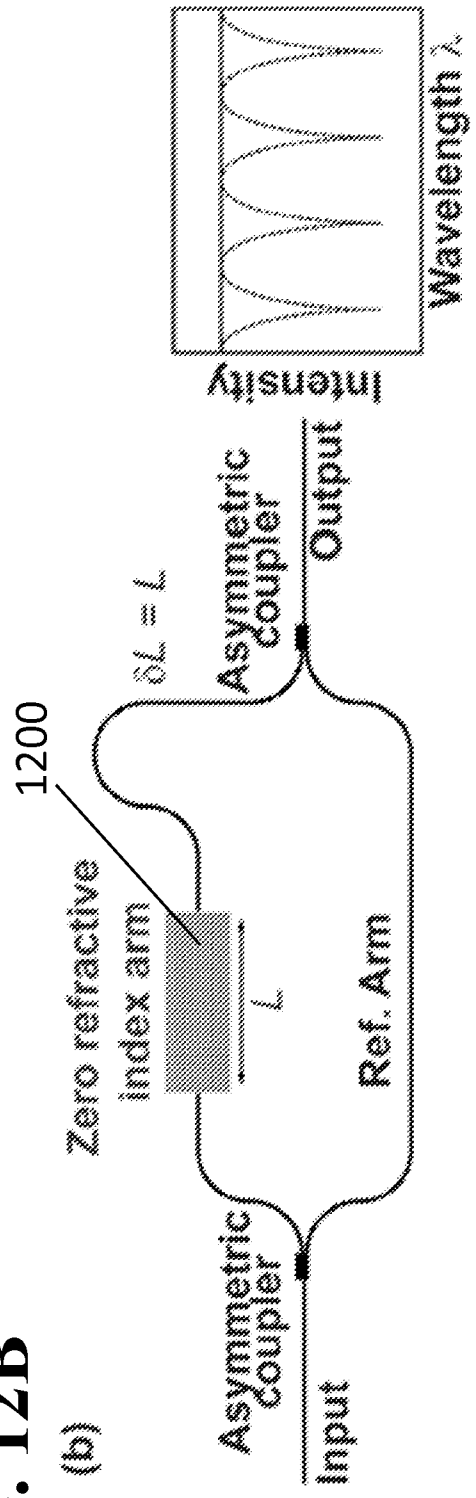

FIG. 13A

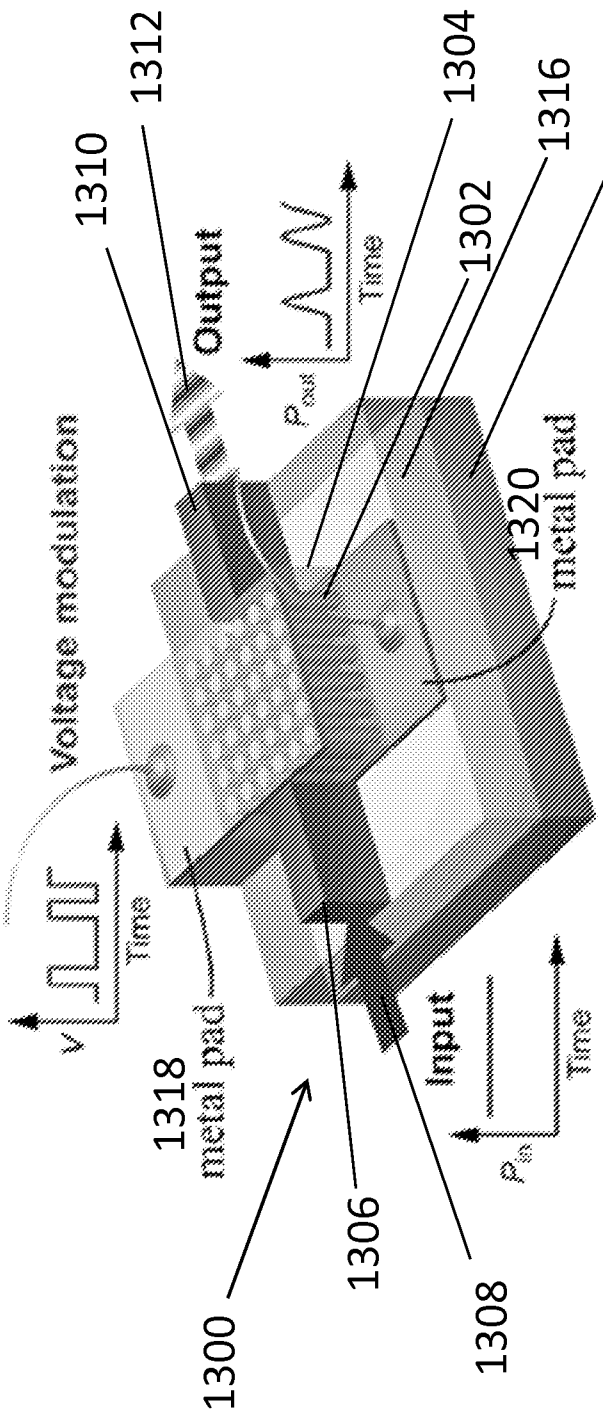

FIG. 13B

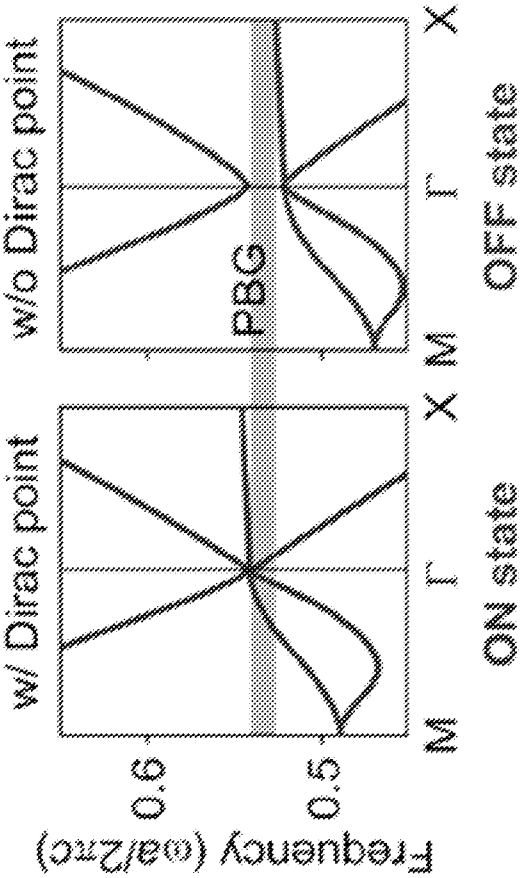

FIG. 13C

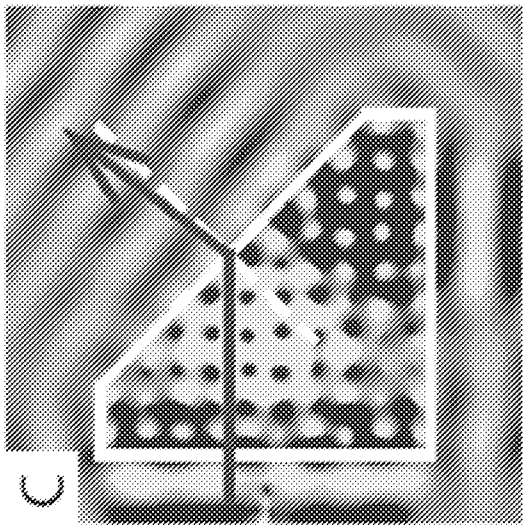

FIG. 14C

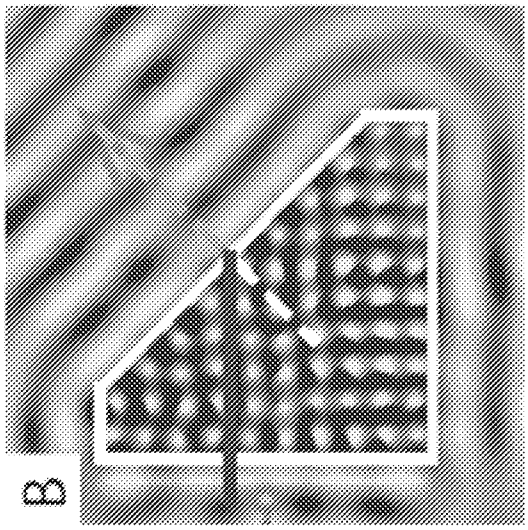

FIG. 14B

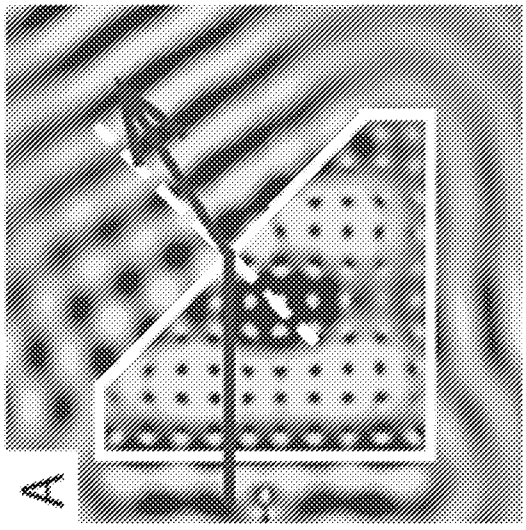

FIG. 14A

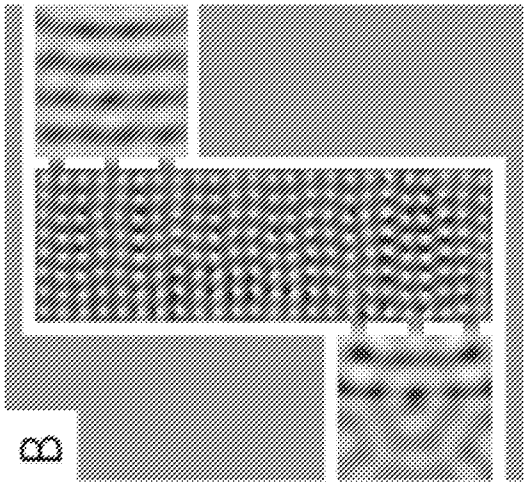

FIG. 15B

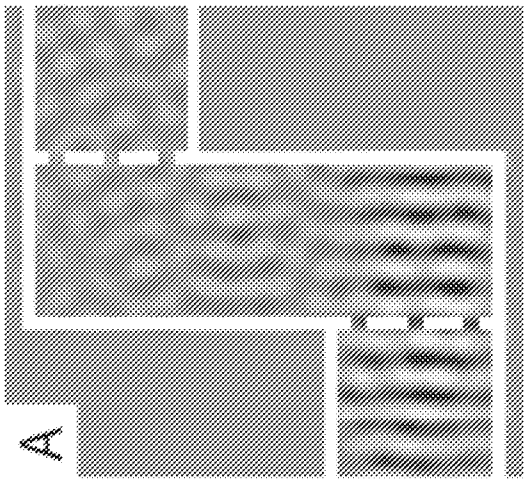

FIG. 15A

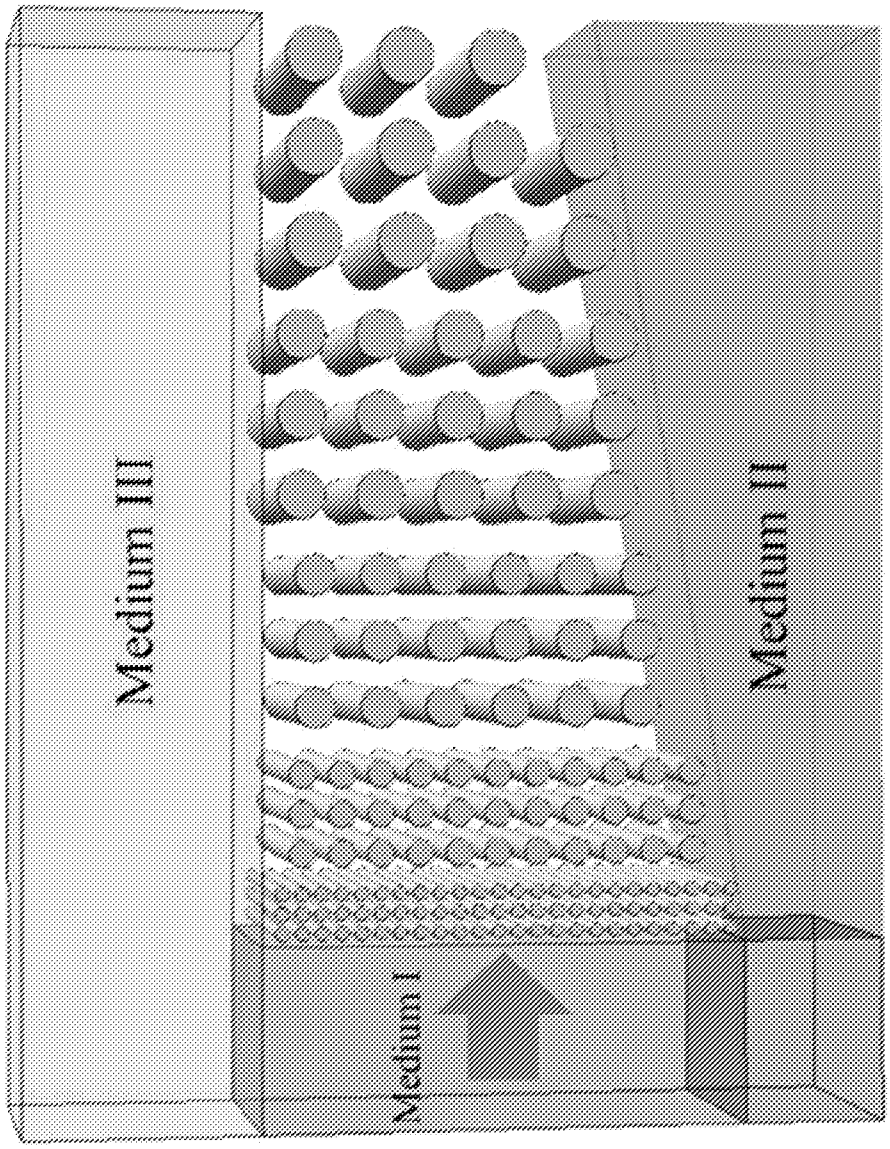

FIG. 16

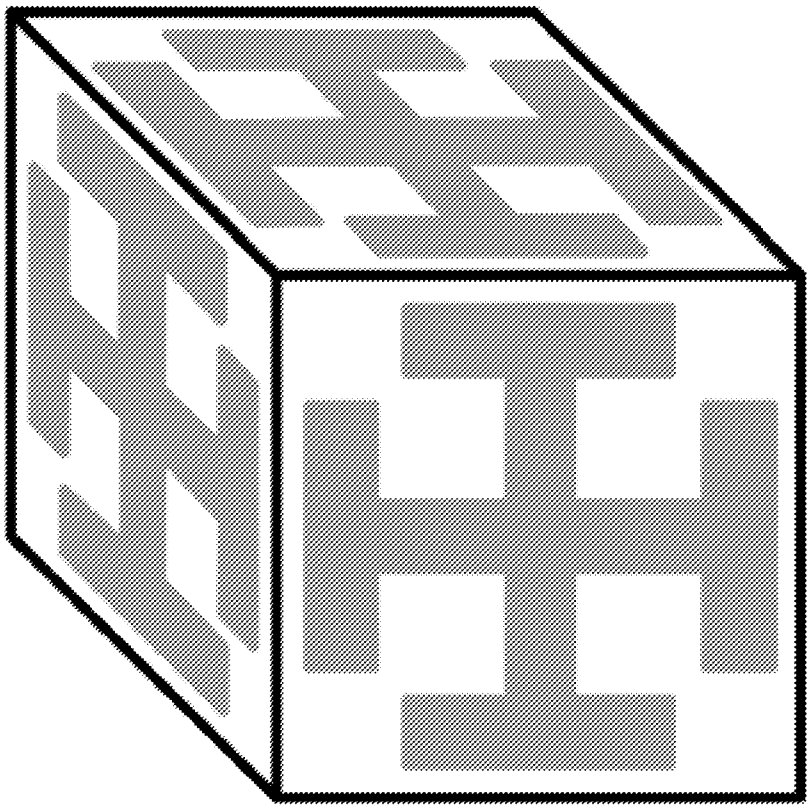

FIG. 17

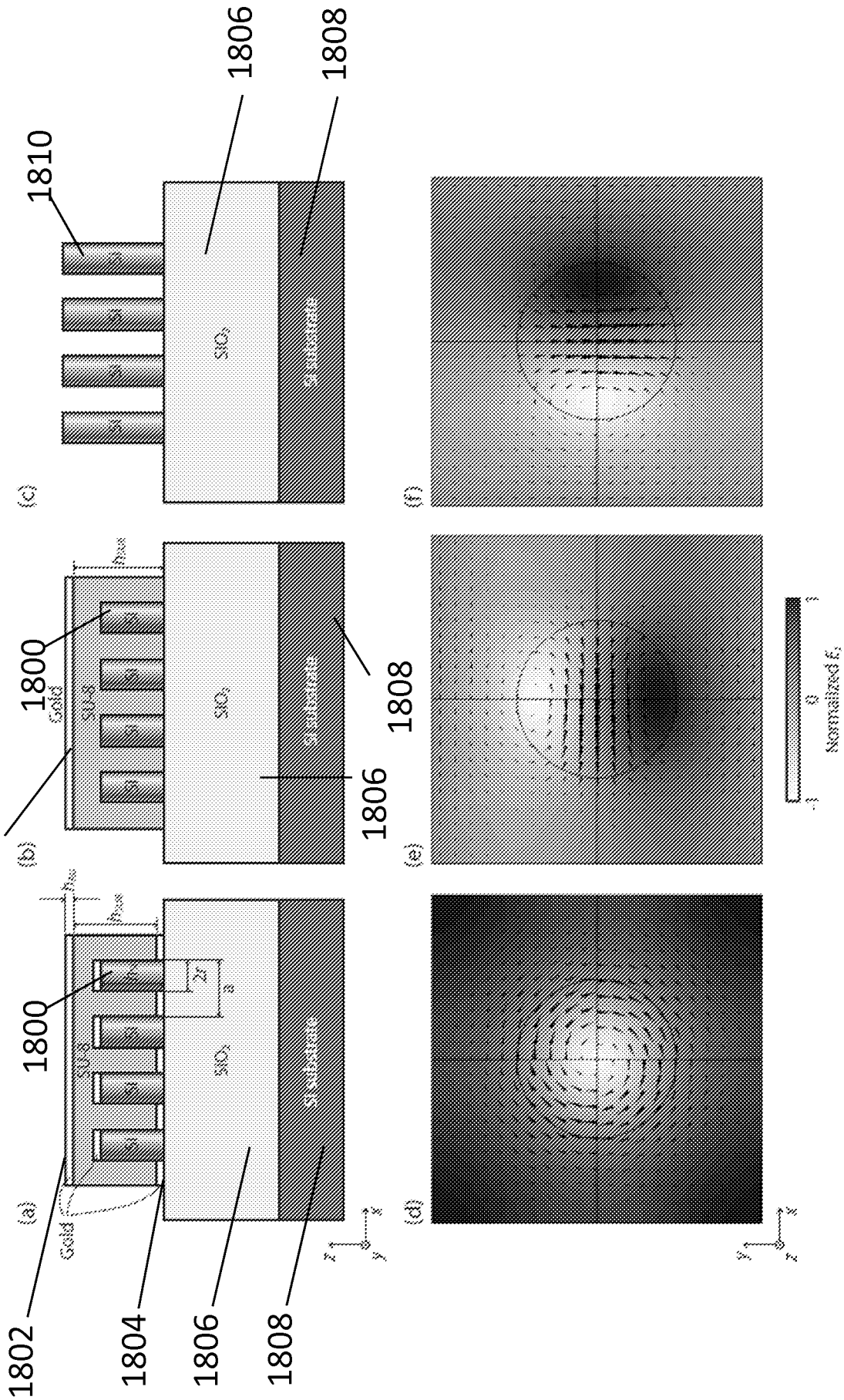

FIG. 18A FIG. 18B FIG. 18C

FIG. 18D FIG. 18E FIG. 18F

FIG. 19A

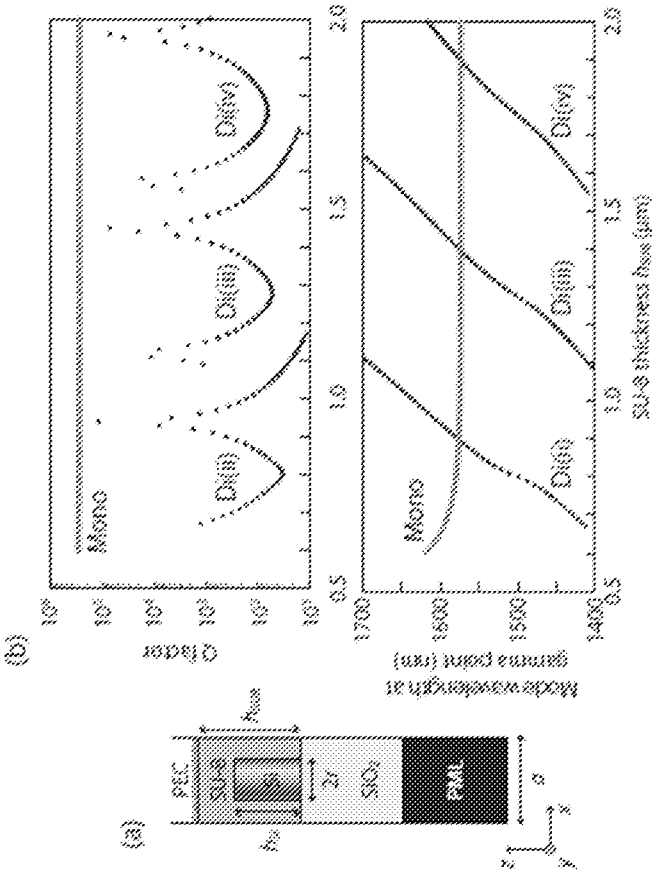

FIG. 19B

FIG. 19C

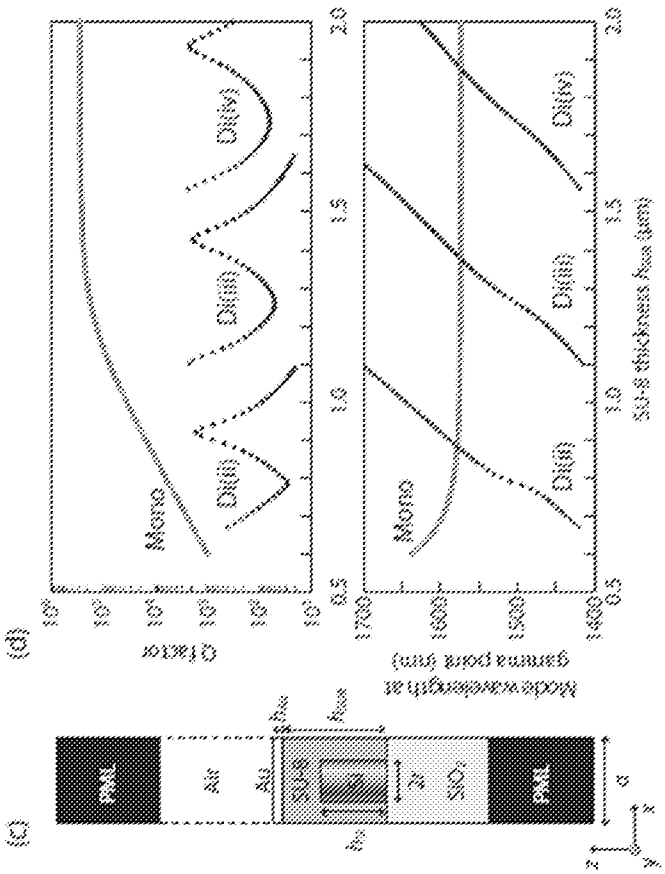

FIG. 19D

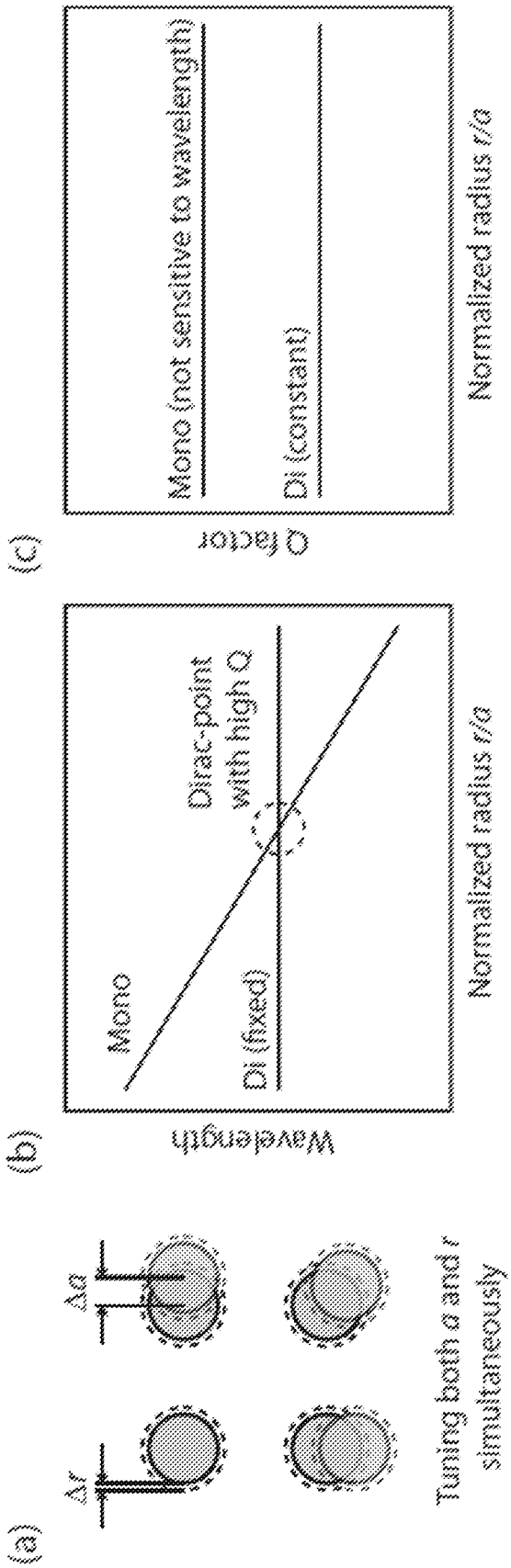

FIG. 20A

FIG. 20B

FIG. 20C

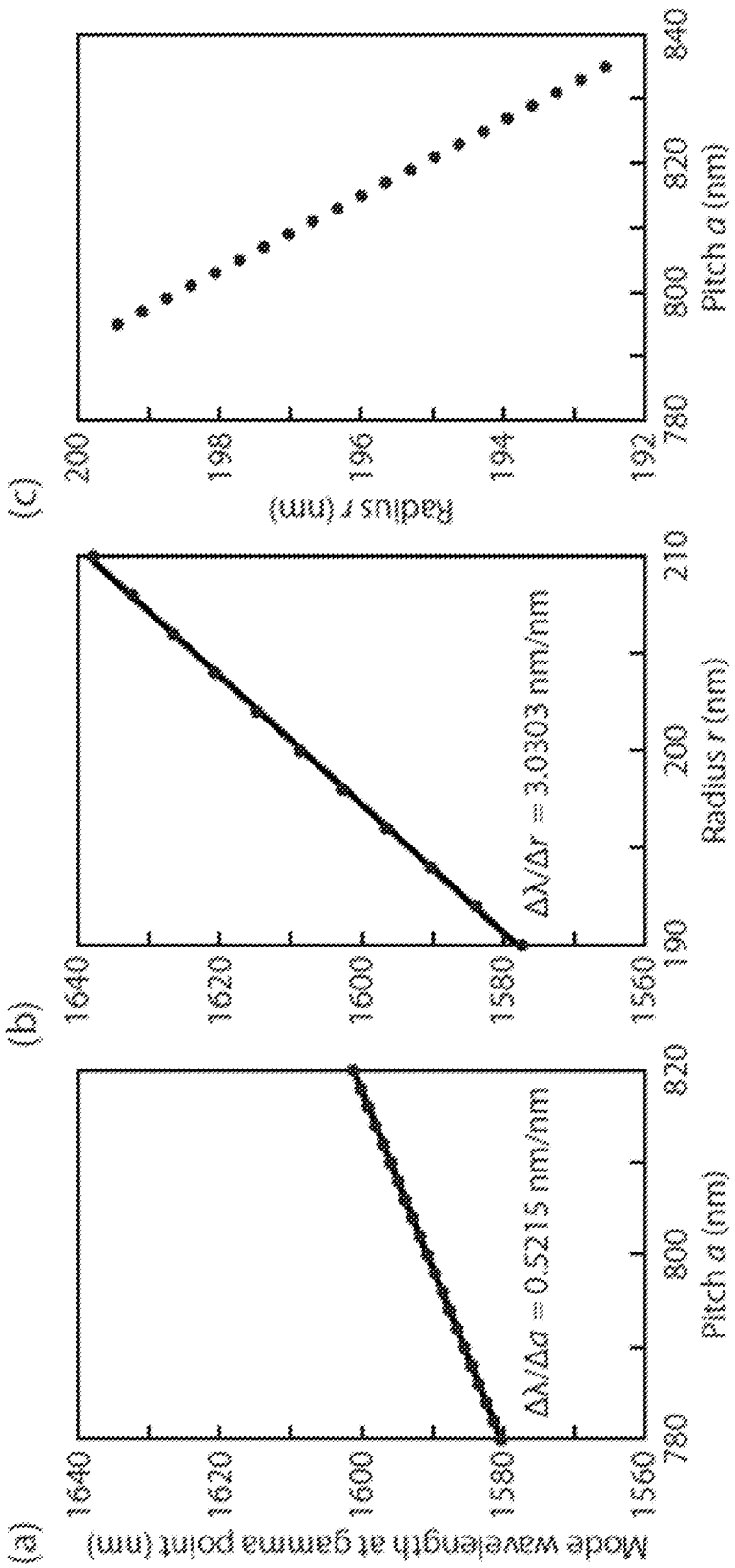

FIG. 21A

FIG. 21B

FIG. 21C

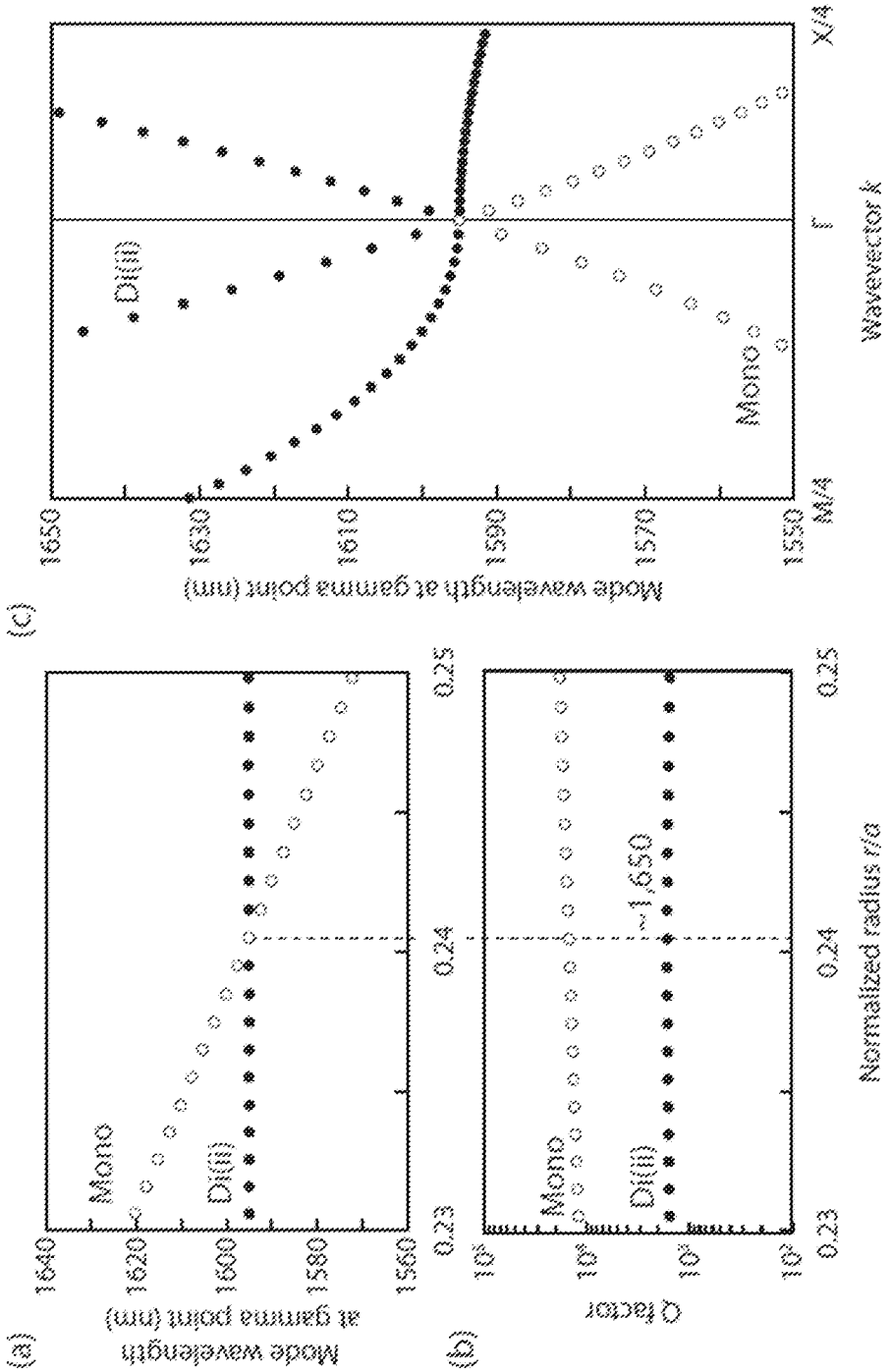

FIG. 22A

FIG. 22B

FIG. 22C

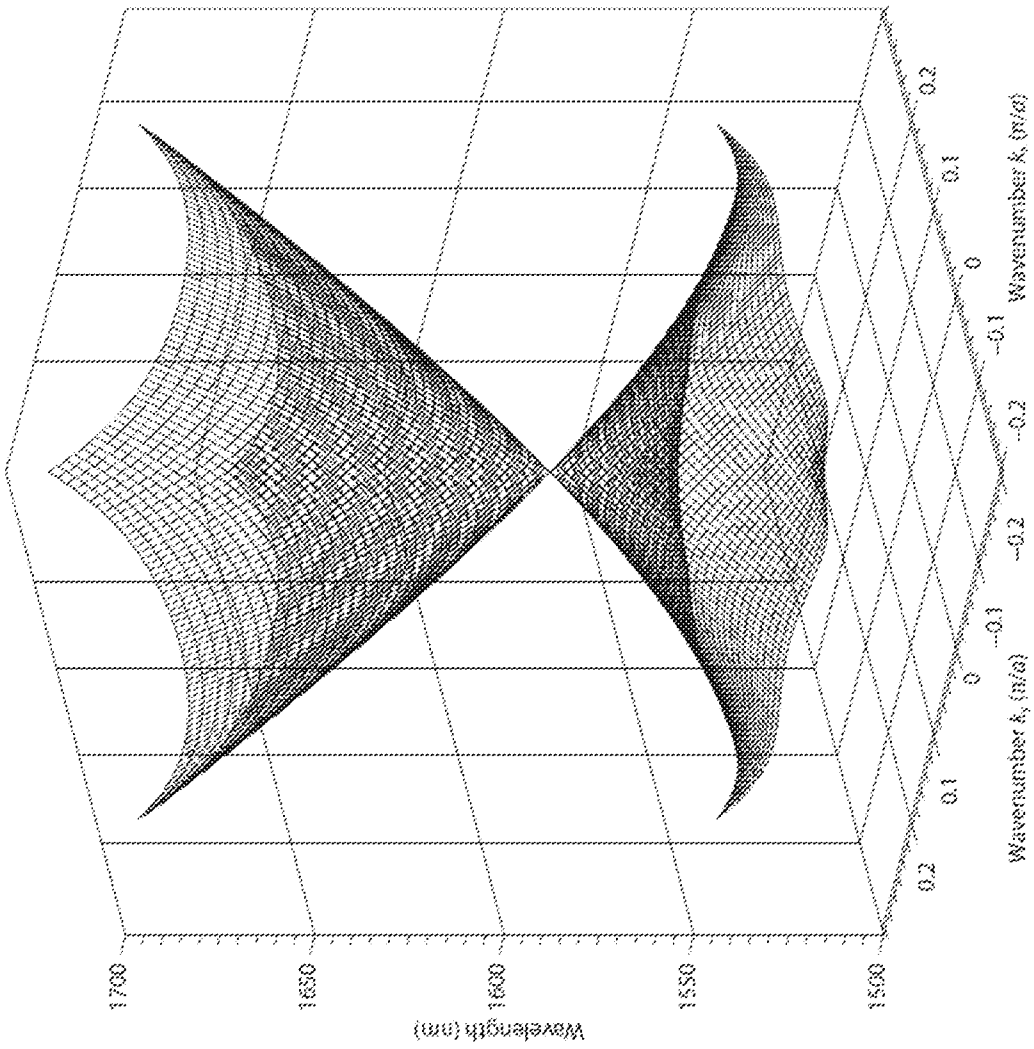
1700
1650
1600
1550
1500
Wavelength (nm)
0.2
0.1
0
−0.1
−0.2
Wavenumber k_x (π/a)
0.2
0.1
0
−0.1
−0.2
Wavenumber k_y (π/a)

FIG. 23

FIG. 24A

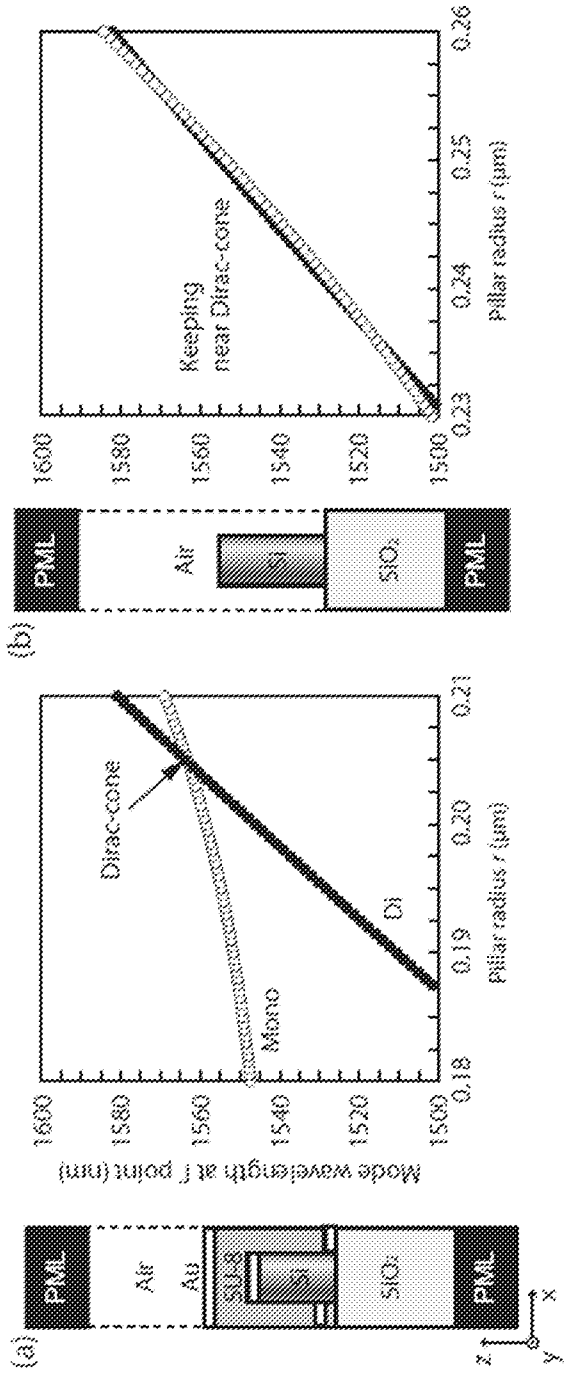

FIG. 24B

FIG. 24C

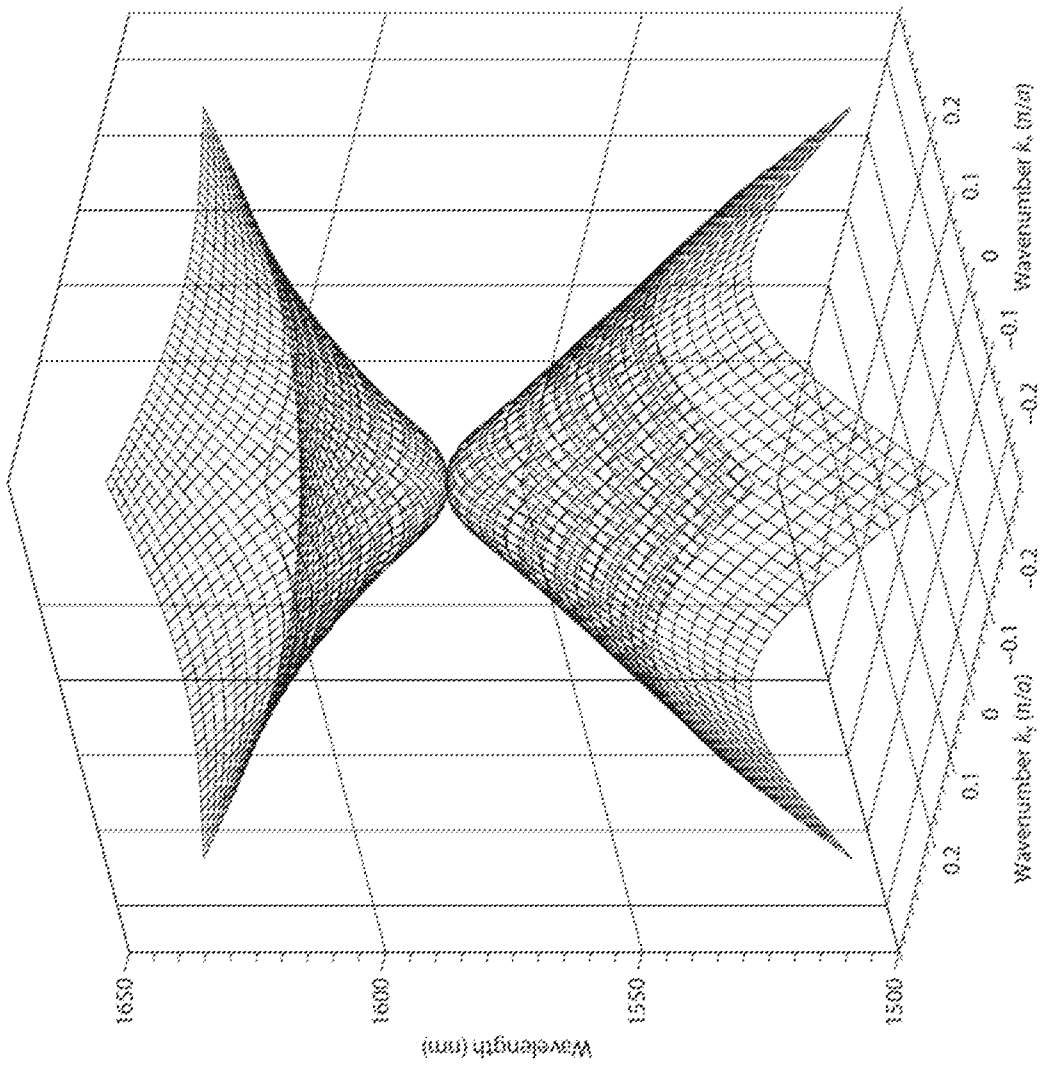
Wavelength (nm)
1650
1600
1550
1500
Wavenumber k_x (rad/m)
0.2
0.1
0
-0.1
-0.2
Wavenumber k_y (rad/m)
0.2
0.1
0
-0.1
-0.2

FIG. 25

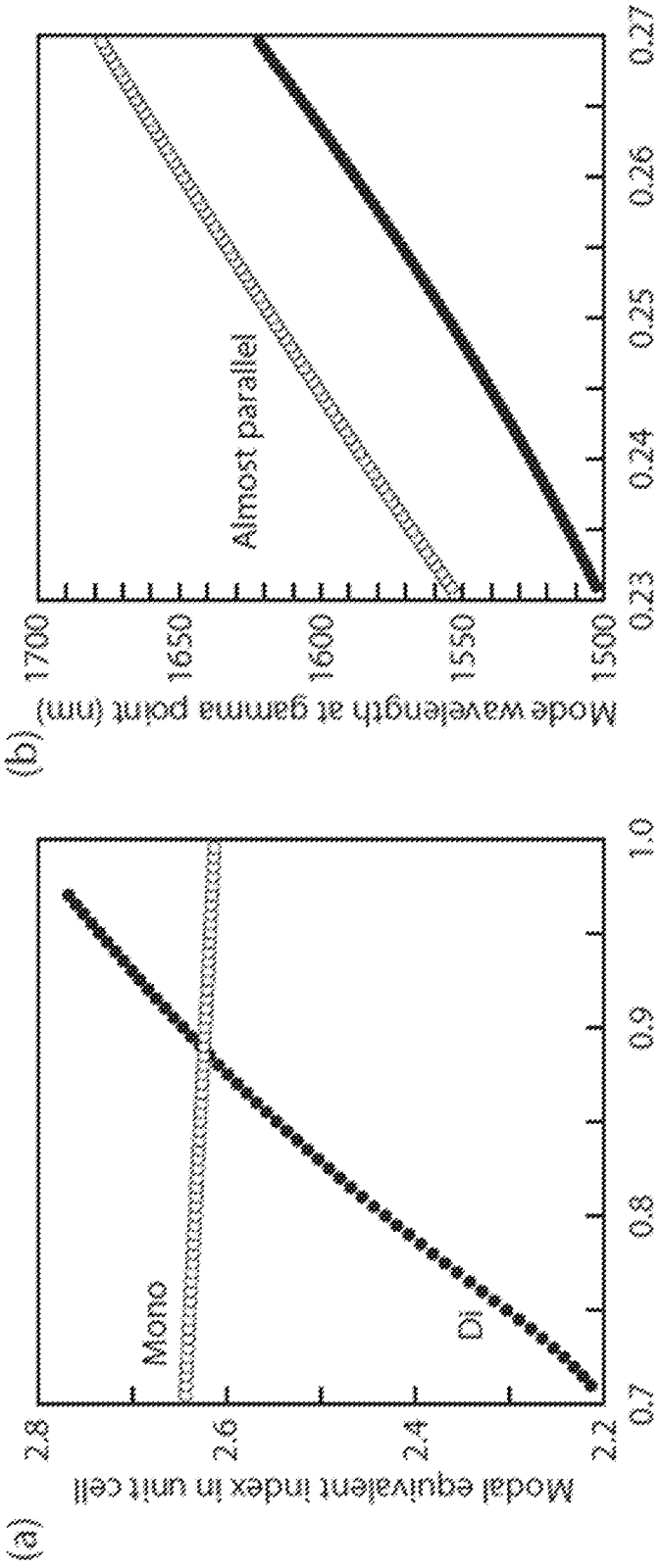

FIG. 26A

FIG. 26B

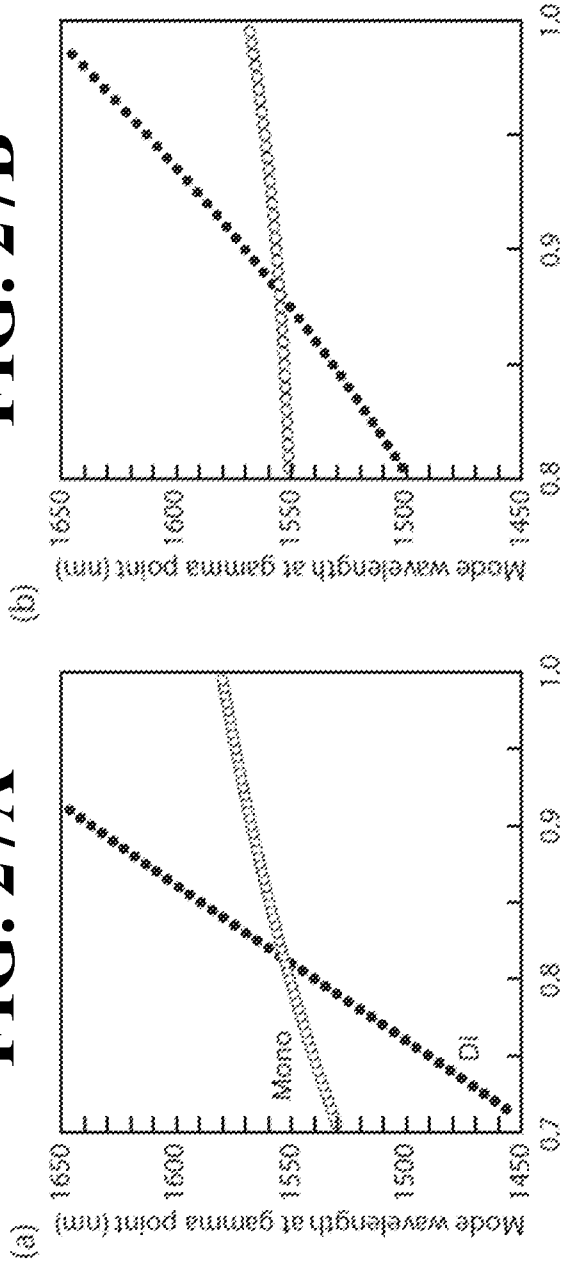

FIG. 27A

FIG. 27B

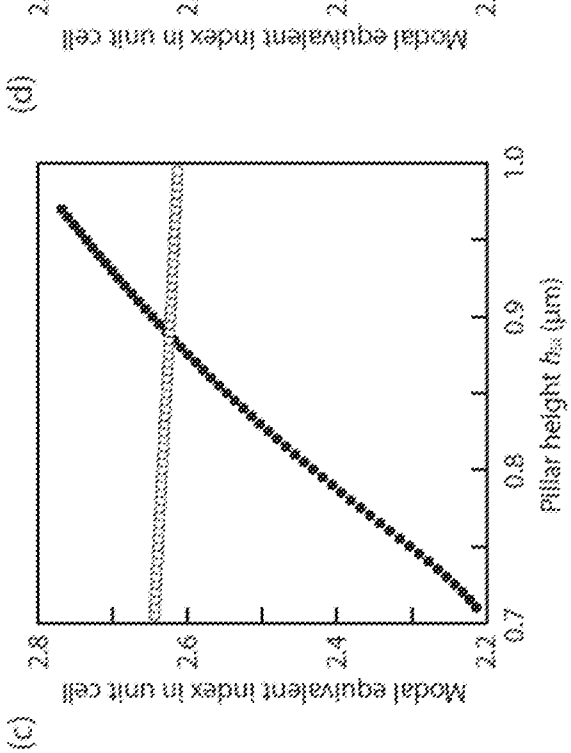

FIG. 27C

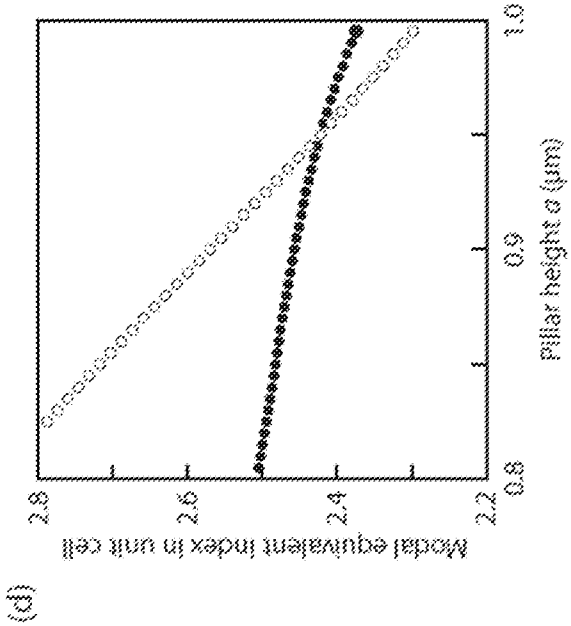

FIG. 27D

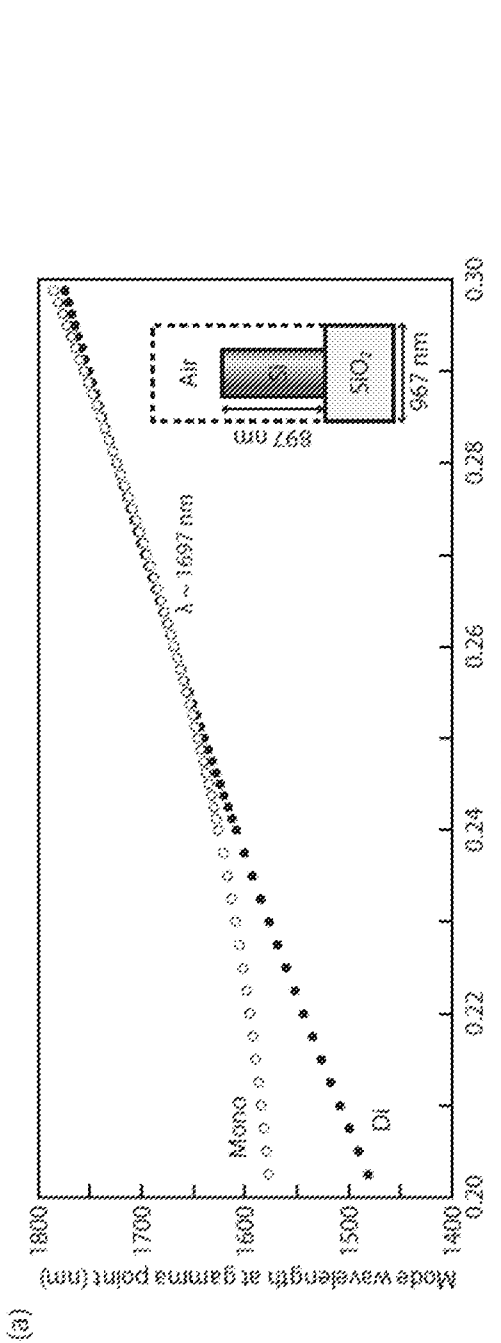

FIG. 28A

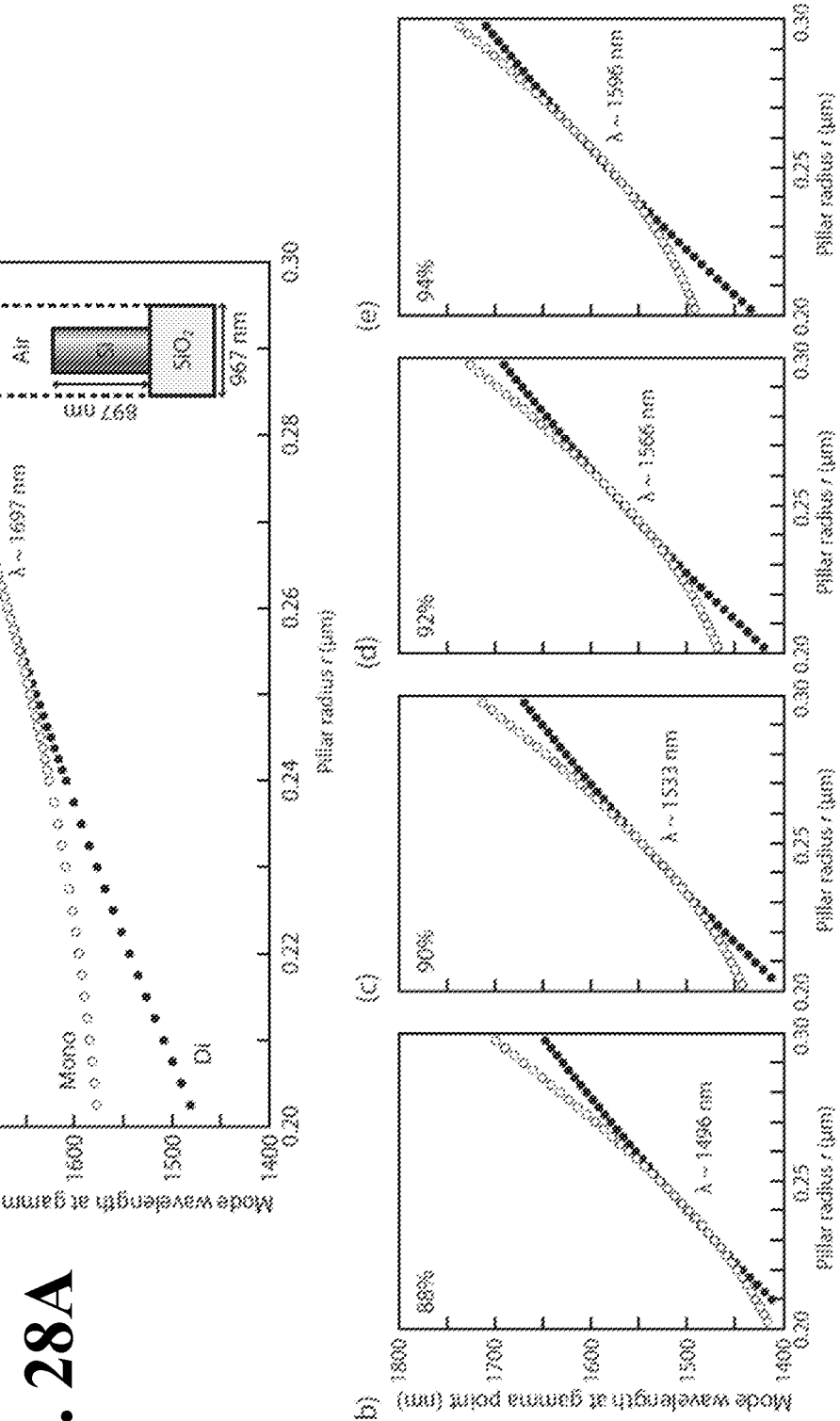

FIG. 28B FIG. 28C FIG. 28D FIG. 28E

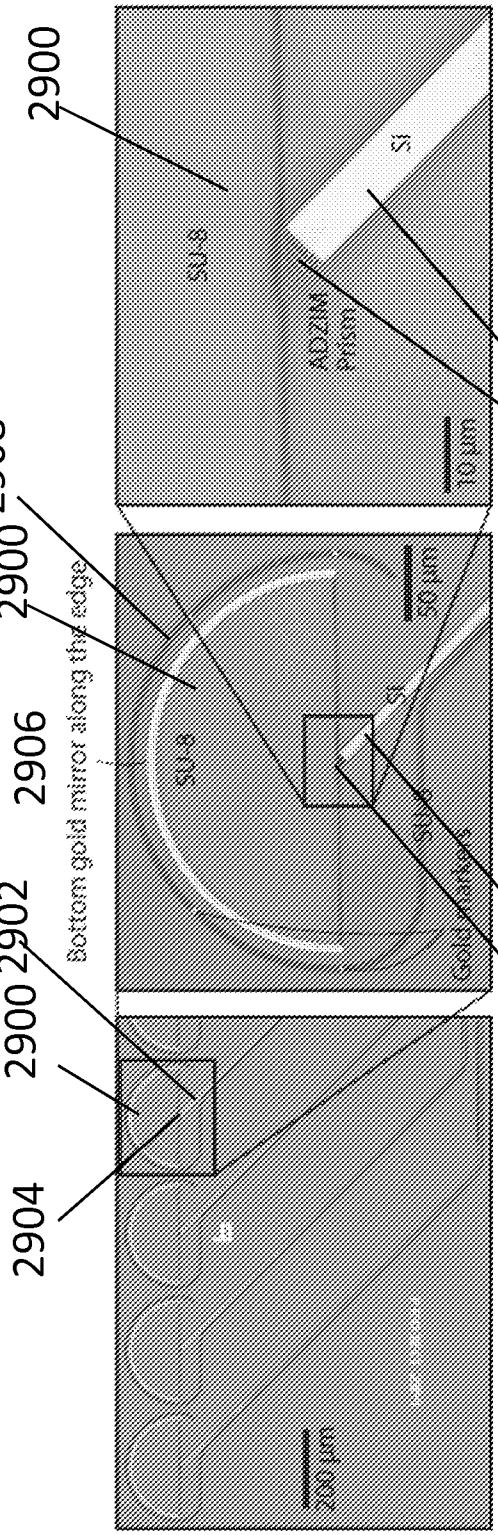

FIG. 29A FIG. 29B FIG. 29C

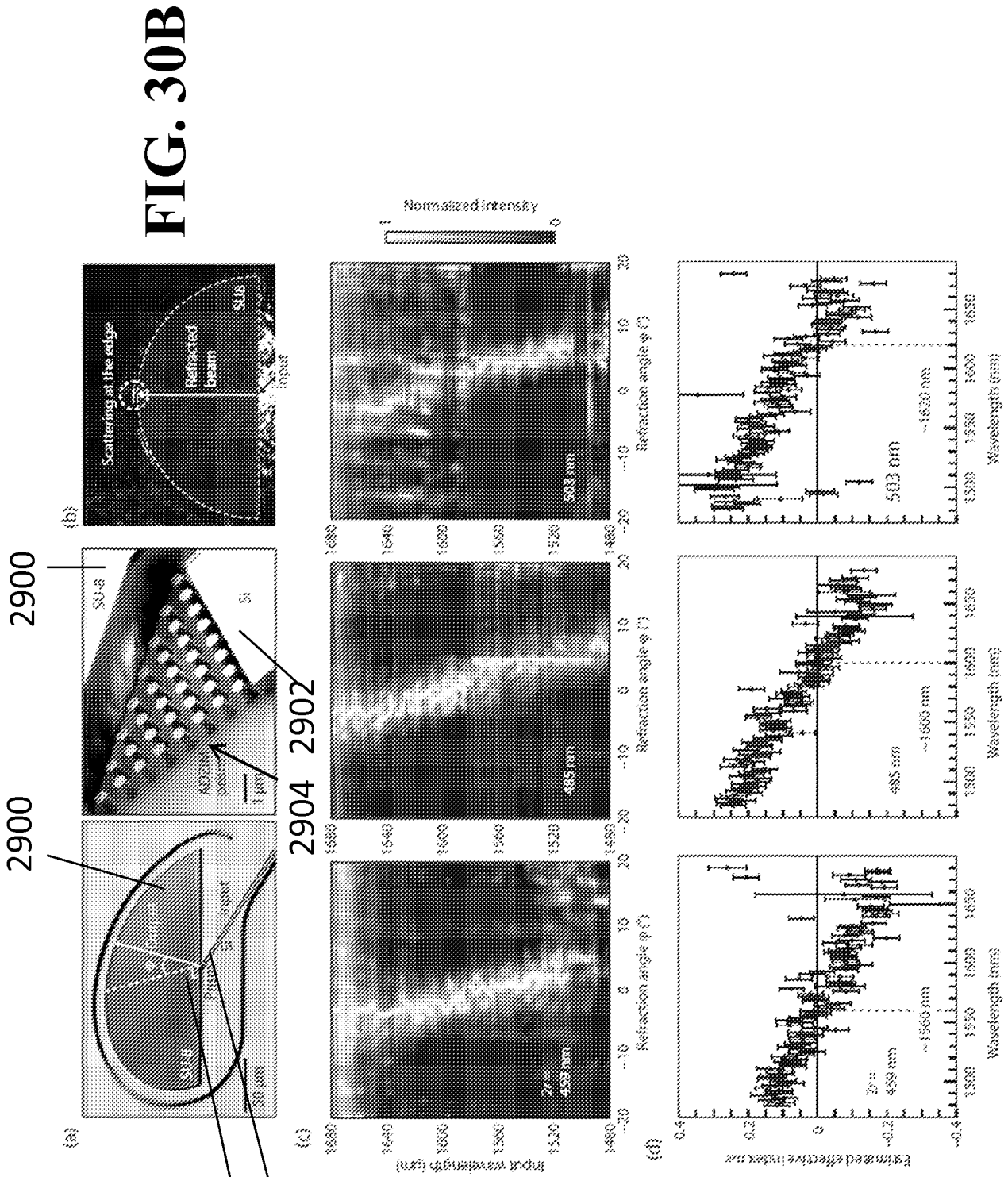

FIG. 30A

FIG. 30B

FIG. 30C

FIG. 30D